Evaluating land surface albedo estimation from Landsat MSS, TM, ETM +, and OLI data based on the unified direct estimation approach

Tao He[a,b,*], Shunlin Liang[b], Dongdong Wang[b], Yunfeng Cao[c], Feng Gao[d], Yunyue Yu[e], Min Feng[b]

[a] School of Remote Sensing and Information Engineering, Wuhan University, Wuhan, Hubei 430079, China
[b] Department of Geographical Sciences, University of Maryland, College Park, MD 20742, USA
[c] College of Forestry, Beijing Forestry University, Beijing 100083, China
[d] USDA-ARS Hydrology and Remote Sensing Laboratory, Beltsville, MD 20705, USA
[e] NOAA/NESDIS/Center for Satellite Applications and Research, Riverdale, MD 20737, USA

ARTICLE INFO

ABSTRACT

Surface albedo is widely used in climate and environment applications as an important parameter for controlling the surface energy budget. There is an increasing need for albedo data to be available for use in applications that require a fine spatial resolution and for validating coarse-resolution datasets; however, such products with long-term global coverage are not available thus far. Existing algorithms for Landsat albedo estimation all require surface reflectance from explicit and reliable atmospheric correction, which may sometimes be unavailable or carry uncertainties due to saturated visible bands or a lack of dense vegetation. In addition, most of the existing algorithms require concurrent clear-sky observations from the Moderate Resolution Imaging Spectroradiometer (MODIS) for bidirectional reflectance distribution function (BRDF) correction, which limited the data availability for Landsat albedo estimation. To overcome these problems, in this study, we adopt the direct estimation approach previously used with coarser resolution data, such as MODIS and Visible Infrared Imaging Radiometer Suite (VIIRS), and apply it to multiple Landsat data obtained by Multispectral Scanner (MSS), Thematic Mapper (TM), Enhanced Thematic Mapper Plus (ETM +), and Operational Land Imager (OLI). By incorporating Landsat spectral response functions and a database of bidirectional reflectance distribution function (BRDF) into radiative transfer simulations, a unified algorithm is developed to estimate surface albedo directly from the Landsat top-of-atmospheric reflectance data obtained by MSS, TM, ETM +, and OLI with few ancillary inputs. To overcome the saturation problems in the visible bands of TM and ETM + over very bright surfaces, a refined approach is employed by using only non-saturated bands. The validation results against ground measurements over various land cover types and climate regions show that our algorithm is effective for both snow-free and snow-covered surfaces and can achieve root-mean-square errors (RMSEs) of not more than 0.034. In addition, we show the high potential of the earlier MSS data for producing consistent surface albedo estimations based on inter-comparison with TM-based results with RMSEs of 0.011–0.017 and R^2 of 0.858–0.963. This long-term, 30-m resolution surface albedo estimation can date back to the early 1980s, which allows for improved understanding of long-term climate change and land cover change effects.

1. Introduction

Land surface albedo is widely used as a controlling factor of the Earth's energy budget by regulating the amount of solar radiation reflected by the surface (Liang et al., 2010). Satellite remote sensing of land surface albedo has continuously improved during the past three decades, and many satellite products are now available for coarse resolution climate modeling applications (He et al., 2014a; Li and Garand, 1994; Liang et al., 2013; Martonchik et al., 1998; Muller et al., 2012; Pinty et al., 2000; Popp et al., 2011; Riihela et al., 2013; Schaaf et al., 2002; Wang et al., 2013).

Although satellite albedo products with a fine spatial resolution are in high demand, which describes the spatial heterogeneity of land surface albedo and represents the changes in albedo due to small-scale land cover changes (Roman et al., 2013; Shuai et al., 2011; Shuai et al., 2014). However, no such products with long-term global coverage are available. Factors such as scale differences between coarse-resolution data and ground measurements have prevented more accurate assessment of existing satellite data for research on climate modeling in the absence of fine-resolution data (e.g., Burakowski et al., 2015; Roman

et al., 2013; Wang et al., 2012). As a result of the free access to Landsat data (Woodcock et al., 2008) and recent technical advancements in data processing (e.g., Masek et al., 2006), there is the potential for albedo data to be used in applications that require data at finer spatial resolutions, such as urban environmental assessment (Zhou et al., 2012), agricultural monitoring (Gao et al., 2014; Li and Fang, 2015), forestry management (Kuusinen et al., 2014; Vanderhoof et al., 2014), and ecosystem functioning evaluation (Lagomasino et al., 2015).

Physically-based or semi-empirical algorithms based on the temporal accumulation of angular samples have been widely used with coarse-resolution data, such as the algorithms developed for Moderate Resolution Imaging Spectroradiometer (MODIS) data (Lyapustin et al., 2011; Schaaf et al., 2002). For data from fine-resolution satellite sensors (e.g., Landsat) it is difficult to apply such physically-based or semi-empirical algorithms due to insufficient angular samples from one sensor within a short period for capturing surface anisotropy caused by the reduced revisit frequency. Previous studies reported that failure to correct the effects of surface bidirectional reflectance distribution function (BRDF) can introduce errors of up to 60% in fine-resolution data (e.g., Gao et al., 2014), which demonstrates the importance of converting surface directional reflectance to albedo.

To attempt to correct for the BRDF effects without BRDF model inversion and to produce land surface albedo from Landsat data, several previous studies have shown promising results over snow-free surfaces. Shuai et al. (2011) proposed a method of using the concurrent 500 m MODIS albedo/BRDF product to convert Landsat surface reflectance to albedo, by taking the advantage of surface BRDF information derived from coarse-resolution data which cannot be obtained directly from Landsat data. Two general assumptions were made in their method. First, land surface was assumed to be invariant within the 16-day compositing period of MODIS data. Second, the ratio of reflectance to albedo was assumed to be the same between a Landsat pixel and a MODIS pixel with the same land cover type. To avoid the selection of homogeneous MODIS pixels at Landsat spatial resolution and to reduce the gridding artifacts in MODIS 500 m data reported in Tan et al. (2006), Franch et al. (2014) presented a two-step method for Landsat albedo estimation. The first step is to estimate surface BRDF from the MODIS 0.05° surface reflectance data, assuming a stable BRDF shape with changing reflectance magnitude during a short period (Vermote et al., 2009) in which the seasonal BRDF shape variation is derived from the normalized difference vegetation index (NDVI). In the second step, the BRDF from MODIS data is then disaggregated to the corresponding Landsat pixels with the help of a land cover map. Both methods (Franch et al., 2014; Shuai et al., 2011) rely on clear-sky MODIS data close to Landsat acquisition date to produce accurate snow-free albedo estimation with root-mean-square errors (RMSEs) of 0.015–0.024; however, they are sometimes not applicable when clear-sky MODIS data are not available and are limited for application past 2000. In addition, a reliable atmospheric correction is required to generate surface reflectance from Landsat TOA reflectance (Masek et al., 2006), which is then used for albedo estimation. For sensors prior to Landsat-8 Operational Land Imager (OLI), Landsat-based atmospheric correction sometimes can be unreliable when accurate aerosol loadings are not available (Ju et al., 2012) with a possibility to obtain inaccurate albedo estimation.

For snow-covered albedo estimation, two studies have estimated shortwave albedo based on the method proposed in Shuai et al. (2011), which was originally designed for snow-free albedo estimation. Wang et al. (2012) reported biases from − 0.076 to 0.01 of isotropic version surface shortwave albedo estimated from non-saturated Landsat TM data versus ground measurements obtained at the Barrow site, in which Landsat albedo was used for MODIS albedo product inter-comparison over snow-covered surfaces. A recent study reported an RMSE of 0.043 for the snow albedos estimated from Landsat 8 data (Wang et al., 2016). While the reported snow-covered albedo estimation accuracies are reasonably good, it is difficult to apply such approaches to the Landsat

Thematic Mapper (TM) and Enhanced Thematic Mapper Plus (ETM +) data acquired over highly reflective surfaces because of saturation issue (Wang et al., 2016; Wang et al., 2012), which were designed with dynamic range to accommodate the variance in reflectivity over various surface types. However, the data of the visible bands are often saturated if the sensor is put in the low-gain mode (Karnieli et al., 2004). We found that the default AOD values were used (e.g., 0.06 over Greenland and 0.01 over the US) in the atmospheric correction for saturated scenes when producing the current version of the Landsat surface reflectance products, which may lead to biased surface reflectance estimation in certain regions. Benefiting from the improved radiometric characteristics, the OLI onboard Landsat 8 is not affected by the saturation issue.

To satisfy an increasing demand for studies on the surface energy budget related to long-term climate change (e.g., Ghimire et al., 2014; O'Halloran et al., 2012), the development of accurate and consistent surface albedo products is important. However, challenges in such product development includes but are not limited to difficulties in estimating surface albedo resulting from ephemeral snow at mid- to high-latitude regions and inter-sensor calibration of coarse-resolution data such as the Advanced Very High Resolution Radiometer (AVHRR) (Molling et al., 2010). Unlike AVHRR sensors onboard different satellites, each of Landsat satellites has a relatively long temporal coverage. In terms of its data consistency, long-term assessment of Landsat sensor calibration has shown that the sensor degradation has been well characterized for Landsat data since the 1980s (Chander et al., 2009; Kim et al., 2014), which enables the use of the legacy data in the determination of surface albedo. To extend Landsat albedo products to the pre-MODIS era for a comprehensive understanding of albedo consequences of forest disturbance and recovery at a fine spatial resolution, a BRDF look-up table (LUT) approach was proposed by considering factors including land cover type, forest disturbance age and severity, and the topography over the United States, as well as high-quality albedo/BRDF information from the MODIS BRDF product (Shuai et al., 2014). RMSE of 0.016 with measured albedo values ranging from 0.06 to 0.14 was achieved based on validation against tower measurements at six forest sites showed, which enabled extending Landsat albedo estimation back to mid-1980s as long as all the necessary information required by the forest disturbance BRDF LUT is available.

All the existing approaches for deriving surface albedo from Landsat data all require surface reflectance derived from a reliable atmospheric correction. However, it is unlikely to generate accurate surface reflectance when dark dense vegetation was not present in the scene or saturation occurred to visible bands. Applying the direct estimation approach to Landsat data could overcome such limitation; meanwhile it enables the exploration of possible means for further extending the albedo data records to the pre-TM era. This method has been developed and refined for data from several satellite platforms (He et al., 2015a; He et al., 2015b; Liang et al., 2003; Qu et al., 2014; Wang et al., 2013). The basic principle of this approach (Liang, 2003; Liang et al., 1999; Liang et al., 2005) is to employ the empirical relationship built from extensive radiative transfer simulations in estimating surface albedo from top-of-atmosphere (TOA) observations. To mitigate non-linearity issues, the empirical relationships between TOA observations and surface albedo are established on an angular-bin basis. Following this approach, an assumption of a stable surface BRDF during a certain period or an explicit atmospheric correction is unnecessary.

The main objective of this paper is to evaluate a unified approach for estimating surface albedo from Landsat TOA reflectance over different land cover types without being constrained by any concurrent high-level satellite products as the inputs. This method can use the legacy data obtained from the entire Landsat satellite series as long as their radiometric and geometric calibration accuracies permit. The algorithm is validated at different locations over various land cover types. These efforts will allow for an improved understanding of surface albedo changes that occur in finer scales, such as forest cover changes,

agricultural expansion, and urban environment changes. Moreover, the results can be used to investigate the uncertainties in coarse-resolution datasets over heterogeneous landscapes.

In this study, several efforts for evaluating the unified approach for Landsat surface albedo estimation have been made. A unified approach previously developed for coarse resolution data is adopted and applied to the Landsat data series including the Multispectral Scanner (MSS), TM, ETM +, and OLI without the need for any concurrent high-level satellite products for correcting atmospheric and surface BRDF effects. The Landsat surface albedo estimates are then evaluated against ground measurements obtained from sites over various land cover types and climate regions. Moreover, the application of the direct estimation approach is demonstrated for the estimation of spectral albedo as well as other broadband albedos, including visible albedo.

2. Methods

2.1. Landsat satellite data

Landsat satellite data have been available since the early 1970s. Onboard the early series Landsat satellites 1–5 were MSS sensors with four spectral bands in the visible to near-infrared spectral range at an approximate spatial resolution of 60 m; band 4 of Landsat 5 MSS failed in 1995. The TM onboard Landsat 4 and 5 satellites with seven spectral bands covered the shortwave range at a resolution of 30 m from 1984 to 2011. Landsat 7, launched in 1999, carried the ETM + with spectral bands and spatial resolution similar to those of the TM. To mitigate the saturation problem over bright surfaces at high latitudes, ETM + was designed to have two modes including a low-gain mode, which is similar to TM, and a high-gain mode (Masek et al., 2001). ETM + had been working well until May 2003, when the failure of the scan line corrector (SLC) resulted in image data gaps. The most recent satellite in the Landsat family, Landsat 8, was launched in February 2013 carrying a 30-m resolution OLI with improved quantization and calibration along with two additional optical bands for improved monitoring of aerosols and cirrus clouds. The spectral response functions of the four sensors onboard Landsat 5, 7, and 8 satellites were obtained from the U.S. Geological Survey (USGS). The band information is shown in Table 1.

Radiometric calibration efforts have been conducted during the past three decades for the sensors onboard the Landsat satellites with a nominal calibration accuracy of 5% (Chander et al., 2009; Thome et al., 1997). The geolocated and terrain-corrected product, Level 1T (L1T) is available for each of the sensors, with a geolocation uncertainty of less than a half pixel for TM, ETM +, and OLI. The relative geolocation error is slightly larger for MSS data, sometimes up to 2 pixels (Tucker et al., 2004).

In this study, we downloaded all available Landsat data from the 1990s to 2016 with matched ground measurements; Section 2.3 presents details on Landsat data selection. To mitigate issues such as reduced data quality, clouds, and reduced geolocation accuracy, the L1T data with only a small amount of cloud coverage and the highest data quality according to the USGS website, with a quality flag of 9, were used for validation purposes. TOA reflectance data were calculated by using the coefficients included in the Landsat data L1T metadata files.

2.2. MODIS BRDF database and surface spectrum

MODIS has been generating surface albedo/BRDF products since 2000 (Schaaf et al., 2002). In the MODIS algorithm, surface reflectance data collected every 16 days at 8-day intervals were used to fit the Ross-Li kernel models, expressed as:

$$\rho(\theta_s, \theta_v, \varphi) = f_{iso} + f_{geo}k_{geo}(\theta_s, \theta_v, \varphi) + f_{vol}k_{vol}(\theta_s, \theta_v, \varphi) \quad (1)$$

where $\rho(\theta_s, \theta_v, \varphi)$ is the surface reflectance with a solar zenith angle θ_s, view zenith angle θ_v, and relative azimuth angle φ; k_{geo} and k_{vol} are the kernels representing the geometric optical mutual shadowing and volumetric scattering components of the surface reflectance, respectively; f_{geo} and f_{vol} are the weights of the two components; and f_{iso} is the isotropic reflectance component.

A BRDF database was built from the multiyear 500 m MODIS albedo products (MCD43A Collection 5). From a wide range of land cover types from the MODIS land cover product (MCD12Q1), 1000 samples of MODIS BRDF data including vegetation, soil, water, and snow/ice were collected. The samples of BRDF data were randomly selected. Three quality check parameters were used to ensure that the selected BRDF data were reliable and accurate: 1) quality flag, selecting data with the highest quality only; 2) spatial homogeneity, using pixels from homogenous land cover; and 3) data range, ensuring that the directional reflectance calculated from the BRDF parameters for all possible viewing geometries were in the range of zero to 1. Each sample represents a set of BRDF parameters for seven MODIS land bands per pixel. The qualified random samples consist of 28% for dense vegetation with NDVI > 0.7 (e.g., dense forest), 47% for vegetation with 0.15 < NDVI < 0.7 (e.g., cropland and grassland), 14% for barren land or sparse vegetation with NDVI < 0.15, 11% for snow, ice, or water. This BRDF database has been used for estimating surface albedo from MODIS (Wang et al., 2015) and VIIRS (Wang et al., 2013; Zhou et al., 2016).

Because of the differences between the spectral response of the MODIS and Landsat bands, direct application of the MODIS BRDF to Landsat data leads to errors. To mitigate this issue, we first collected 245 surface reflectance spectra of vegetation, soil, rock, water, snow, and ice (He et al., 2014b; He et al., 2012) from the USGS (Clark et al., 2007) and Advanced Spaceborne Thermal Emission and Reflection (ASTER) (Baldridge et al., 2009) libraries. The surface spectrum was then used to establish the relationship between MODIS and Landsat bands by assuming that the band conversion coefficients can be applied to both directional reflectance and albedo. Although the Landsat band design of several sensors (TM, ETM +, and OLI) is similar (Table 1), band conversions (Eq. 2.) for each individual sensor are still needed to reduce uncertainties when applying the MODIS BRDF database to Landsat data. Moreover, this approach can be further extended and applied to data from other optical sensors given the linearity of the MODIS Ross-Li kernel-driven models (He et al., 2015a), expressed as.

$$F_i^{Landsat} = \sum_{j=1}^{7} f_j^{MODIS} \cdot a_j \quad (2)$$

where f_j^{MODIS} is the BRDF parameter for MODIS band j, and a_j is the regression coefficient for calculating the BRDF parameter $F_i^{Landsat}$ for Landsat band i. The band conversion coefficients for each Landsat

Table 1
Spectral bands of Landsat 5 Multispectral Scanner (MSS), Landsat 5 Thematic Mapper (TM), Landsat 7 Enhanced Thematic Mapper Plus (ETM +), and Landsat 8 Operational Land Imager (OLI) used for albedo estimation. The spectral response function data were obtained from the U.S. Geological Survey (USGS).

Band	1	2	3	4	5	6	7
MSS	0.50–0.60	0.60–0.70	0.70–0.81	0.81–1.04	N/A	N/A	N/A
TM	0.45–0.52	0.52–0.60	0.63–0.69	0.76–0.90	1.55–1.75	Not used	2.08–2.35
ETM +	0.45–0.52	0.52–0.60	0.63–0.69	0.77–0.90	1.55–1.75	Not used	2.09–2.35
OLI	0.43–0.45	0.45–0.51	0.53–0.59	0.64–0.67	0.85–0.88	1.57–1.65	2.11–2.29

Table 2
Band conversion coefficients and uncertainties in simulated spectral reflectance.

Sensor	Band	a_1	a_2	a_3	a_4	a_5	a_6	a_7	RMSE
MSS	1	0.173	−0.013	0.169	0.671	0	0	0	0.003
	2	0.989	0.010	−0.023	0.024	0	0	0	0.002
	3	0.198	0.956	0	0	−0.280	0.205	−0.080	0.021
	4	0	0.751	0	0	0.349	−0.137	0.040	0.009
TM	1	0.020	−0.023	0.831	0.167	0.011	0	0	0.011
	2	0.277	0	0.022	0.707	−0.009	0	0	0.021
	3	1.070	0	0	−0.073	0	0.020	−0.012	0.006
	4	−0.029	1.007	−0.028	0.067	−0.032	0.014	0	0.007
	5	0	0	0	0	0.064	0.791	0.158	0.019
	7	0	0	0	−0.051	0.213	−0.357	1.127	0.029
ETM +	1	0.016	−0.016	0.899	0.098	0.008	0	0	0.006
	2	0.177	−0.010	0.055	0.778	0	0	0	0.016
	3	1.084	0	0	−0.087	0	0.015	−0.007	0.006
	4	−0.033	1.013	−0.030	0.074	−0.044	0.018	0	0.008
	5	0	0	0	0	0.033	0.857	0.115	0.016
	7	0	0	0	−0.049	0.197	−0.341	1.128	0.027
OLI	1	−0.043	0.018	1.182	−0.161	0	0	0	0.012
	2	0.023	−0.020	0.872	0.121	0.009	0	0	0.008
	3	0.139	−0.004	0	0.867	0	−0.010	0.007	0.011
	4	1.054	0	0.010	−0.065	0	0.005	0	0.004
	5	0.010	0.985	0	−0.016	0.029	−0.012	0	0.003
	6	0.017	−0.021	0	0	−0.009	0.992	0.019	0.014
	7	0	0	0	−0.036	0.192	−0.275	1.074	0.029

sensor are tabulated in Table 2.

2.3. Ground measurements and Landsat data collection strategy

Surface albedo can be estimated from tower measurements of upward and downward solar radiation. In this study, we used the ground data obtained from the networks including Surface Radiation (SURFRAD), AmeriFlux, Baseline Surface Radiation Network (BSRN), and Greenland Climate Network (GC-Net) for validation (Table 3).

SURFRAD sites began obtaining ground measurements of shortwave radiation in 1995 through the support of National Oceanic and Atmospheric Administration (NOAA) Office of Global Programs. SURFRAD network is part of the BSRN. To avoid any confusion in the texts that follow, the BSRN sites in this study refer to the BSRN sites not included in the SURFRAD network hereafter. The SURFRAD data are available at http://www.esrl.noaa.gov/gmd/grad/surfrad/index.html. In January 2009, the data-recording time intervals were reduced from initial averages of 3 min to 1 min. AmeriFlux network is currently supported and managed mainly by the U.S. Department of Energy at Lawrence Berkeley National Laboratory (LBNL) with data available at http://ameriflux.lbl.gov/. Sites from AmeriFlux provide data at 30 min intervals. To match the ground measurements with satellite data, the flux data recorded within ± 30 min of the satellite overpass time were averaged to calculate the ground shortwave albedo. In addition to solar shortwave radiation data, several AmeriFlux sites also provide measurements of downward and upward photosynthetically active radiation (PAR, 400–700 nm) in which the visible albedo data are calculated by same process as that for shortwave albedo. Because the selected sites from both networks are located in North America, where USGS has the best and most complete Landsat data archive throughout the past decades, only the highest-quality Landsat L1T data with nominal zero cloud cover were downloaded for calibration/validation purposes. However, it is noteworthy that scattered clouds remained in some scenes and were later manually removed on a scene-by-scene basis. By using the data from SURFRAD sites, we were able to assess the performance of the direct estimation approach for various Landsat sensors over both snow-free and snow-covered conditions. AmeriFlux data can help us understand the estimation accuracies for both shortwave and visible albedos over sites with different land cover types. The selected AmeriFlux sites in Table 3 have observations for both shortwave and visible albedos; however, the shortwave and PAR flux measurements

for the same site are not always available at the same time. To keep the validation results consistent, only data with simultaneous measurements of shortwave and visible albedos were included in the validation section.

Ground measurements of surface albedo were calculated as the ratio of total upward to total downward radiation. Known as blue-sky albedo, this parameter reflects the actual radiation budget (Roman et al., 2010). In this study, as a result of using MODIS products as training, blue-sky albedo from Landsat was calculated as a combination of black-sky albedo (BSA) and white-sky albedo (WSA) weighted by the diffuse sunlight fraction measured at the stations. When the diffuse sunlight fraction was not available for the station, the value of 0.2 was used as the default. Footprints of the tower measurements (*D*: footprint diameter) were calculated on the basis of the instrument height *H* and effective field of view θ based on Eq. 3 (Roman et al., 2009). Tower height was used to proximate the instrument height in this study. Average values of satellite pixel-level estimation within the tower footprints were used for comparison against ground measurements.

$$D = 2H \cdot \cos\theta \qquad (3)$$

Initiated by the World Climate Research Programme (WCRP), BSRN is an international network for observing surface radiation budget. Its data can be obtained at http://bsrn.awi.de/. By following a data collection strategy of Landsat images similar to that used for SURFRAD and AmeriFlux sites, we selected only clear scenes with small amounts of scattered cloud cover (< 30%) during the temporal range of 1999–2012 when both Landsat data and ground measurements were available for the BSRN sites. Both Landsat TM and ETM + data manually identified as clear-sky at the site locations were included in this study. Validation at the BSRN sites can help demonstrate the performance of the unified algorithm over various land cover types and climate conditions.

Ground measurements of surface shortwave radiation have been collected over Greenland since 1995 at 30 min intervals, which are maintained by a project sponsored by National Aeronautics and Space Administration (NASA) and the National Science Foundation (NSF). The GC-Net data are available at http://cires1.colorado.edu/steffen/gcnet/. The sites over Greenland include two types of snow conditions: permanent snow cover and fluctuating seasonal snow cover. To investigate the capability of the direct estimation algorithm and Landsat data in the surface albedo estimation, we collected Landsat data over

Table 3
Information of ground stations used for validation.

Site name	Network	Latitude (°)	Longitude (°)	Land cover type[a]	Temporal range	Tower height (m)	Number of scenes[b]
BON	SURFRAD	40.0516	− 88.3733	CRO	1995–2016	10	115
DRA	SURFRAD	36. 6232	− 116.0196	OSH	1998–2016	10	237
FPK	SURFRAD	48.3080	− 105.1018	GRA	1995–2016	10	121
GWN	SURFRAD	34.2547	− 89.8729	GRA	1995–2016	10	179
PSU	SURFRAD	40.7203	− 77.9310	CRO	1998–2016	10	47
SXF	SURFRAD	43.7343	− 96.6233	GRA	2003–2016	10	111
TBL	SURFRAD	40.1256	− 105.2378	GRA	1995–2016	10	94
CA-NS1	AmeriFlux	55.8792	− 98.4839	ENF	2001–2005	24	15
CA-NS2	AmeriFlux	55.9058	− 98.5247	ENF	2001–2005	20	11
CA-NS3	AmeriFlux	55.9117	− 98.3822	ENF	2001–2005	10	10
CA-NS5	AmeriFlux	55.8631	− 98.4850	ENF	2001–2005	9	7
CA-NS6	AmeriFlux	55.9167	− 98.9644	ENF	2001–2005	6	8
CA-NS7	AmeriFlux	56.6358	− 99.9483	ENF	2002–2005	6	4
US-ARM	AmeriFlux	36.6058	− 97.4888	CRO	2004–2013	60	72
US-Aud	AmeriFlux	31.5907	− 110.5092	GRA	2002–2011	4	142
US-Bar	AmeriFlux	44.0646	− 71.2881	DBF	2004–2011	30	31
US-Bkg	AmeriFlux	44.3453	− 96.8362	GRA	2004–2010	4	34
US-Blk	AmeriFlux	44.1580	− 103.6500	ENF	2004–2008	24	26
US-Bo1	AmeriFlux	40.0062	− 88.2904	CRO	1996–2008	10	47
US-Bo2	AmeriFlux	40.0061	− 88.2918	CRO	2004–2007	10	18
US-CaV	AmeriFlux	39.0633	− 79.4208	GRA	2004–2010	4	6
US-ChR	AmeriFlux	35.9311	− 84.3324	DBF	2005–2010	60	25
US-FPe	AmeriFlux	48.3077	− 105.1019	GRA	2000–2008	3.5	41
US-Fuf	AmeriFlux	35.0890	− 111.7620	ENF	2007	23	6
US-Fwf	AmeriFlux	35.4454	− 111.7718	GRA	2005–2010	4	29
US-Goo	AmeriFlux	34.2547	− 89.8735	GRA	2002–2006	4	36
US-IB1	AmeriFlux	41.8593	− 88.2227	CRO	2005–2011	4	32
US-IB2	AmeriFlux	41.8406	− 88.2410	GRA	2004–2011	3.76	34
US-MOz	AmeriFlux	38.7441	− 92.2000	DBF	2004–2013	30	59
US-NR1	AmeriFlux	40.0329	− 105.5464	ENF	2006–2013	26	24
US-Ne1	AmeriFlux	41.1650	− 96.4766	CRO	2001–2013	6	81
US-Ne2	AmeriFlux	41.1649	− 96.4701	CRO	2001–2013	6	81
US-Ne3	AmeriFlux	41.1797	− 96.4396	CRO	2001–2013	6	83
US-Pon	AmeriFlux	36.7667	− 97.1333	CRO	1997–2000	4.5	16
US-SRM	AmeriFlux	31.8214	− 110.8661	WSV	2004–2014	7.8	114
US-Shd	AmeriFlux	36.9333	− 96.6833	GRA	1997–2000	4.5	7
US-WBW	AmeriFlux	35.9588	− 84.2874	DBF	2001–2007	44	29
US-Wkg	AmeriFlux	31.7365	− 109.9419	GRA	2004–2014	6.4	155
US-Wrc	AmeriFlux	45.8205	− 121.9519	ENF	2005–2006	85	4
BAR	BSRN	71.3230	− 156.6070	TND	1995–2014	4	16
BOU	BSRN	40.0500	− 105.0070	GRA	1998–2014	300	97
E13	BSRN	36.6050	− 97.4850	GRA	1995–2014	20	48
GVN	BSRN	− 70.6500	− 8.2500	SNW	1995–2016	1.9	30
PAY	BSRN	46.8129	6.9435	CRO	1998–2014	10	50
SYO	BSRN	− 69.0000	39.5833	SNW	2003–2014	1.5	13
TOR	BSRN	58.2700	26.4700	GRA	1995–2014	2	30
SwissCamp	GC-Net	69.5647	− 49.3308	SNW	2000–2012	4	17
JAR1	GC-Net	69.4950	− 49.7039	SNW	2000–2012	4	18
Saddle	GC-Net	65.9997	− 44.5017	SNW	2000–2012	4	13
NASA-E	GC-Net	75.0006	− 29.9972	SNW	1999–2011	4	25

[a] Cropland (CRO); Deciduous Broadleaf Forest (DBF); Evergreen Needleleaf Forest (ENF); Grassland (GRA); Open shrubland (OSH); Snow and ice (SNW); Woody Savannas (WSV); Tundra (TND).

[b] The number of scenes for each site includes only clear-sky observations used for validation in this study.

four sites covering different parts of Greenland, including SwissCamp, JAR1, Saddle, and NASA-E. In particular, validation results demonstrate the algorithm's performance over snow surfaces when the visible bands are saturated. Because of the limited availability of TM data to match ground measurements, only ETM + data were used in the validation analysis. It is noteworthy that the LI-COR200SZ pyranometers used for flux measurements at GC-Net sites have a spectral coverage of 400–1100 nm, which leads to an overestimation in snow albedo values compared with those covering 300–3000 nm (Stroeve et al., 2013; Stroeve et al., 2006). To evaluate the accuracy of snow albedo estimation at GC-Net sites from this study, the 500 m MODIS albedo product with the best quality (quality flag equals to zero) closest to the Landsat acquisition date is included for comparison. The MODIS albedo data with the best quality means that during the 16-day composite period, the majority of the MODIS clear-sky reflectance for the pixel is either snow-free or snow-covered with a BRDF model fitting error

below a certain threshold (Shuai et al., 2008).

2.4. Direct estimation approach

Surface albedo can be calculated through angular and spectral integration of surface directional reflectance, the former of which is prescribed by a BRDF model (Eq. 1). However, the satellite sensor observes the TOA signal (e.g., TOA reflectance) modulated by the surface and atmospheric conditions through a physically-based radiative transfer. Without accurate estimation of atmospheric condition, surface reflectance either cannot be estimated from an atmospheric correction or contains large error, making it difficult to obtain surface albedo. To overcome this issue, Liang et al. (1999) proposed a statistical method, the so-called direct estimation approach, to estimate surface albedo directly from TOA reflectance without requiring atmospheric correction. The empirical relationship was built through linear regression

upon the simulated surface albedo and TOA reflectance from extensive radiative transfer simulations under various prescribed conditions of surface and atmosphere. This approach was later improved by considering the surface BRDF effects with regression coefficients built under different viewing geometries to mitigate errors from non-linearities (Liang et al., 2005; Wang et al., 2013).

The direct estimation approach was originally developed to derive the surface shortwave albedo from TOA reflectance based on a statistical relationship established from radiative transfer simulations. Based on the increasing need for albedo availability in the narrow spectral domain, we extended the statistical relationship to generate albedos covering the spectral bands and three broadbands, including the visible (300–700 nm), near-infrared (NIR; 700–3000 nm), and total shortwave ranges (300–3000 nm) based on the following linear equation:

$$\alpha_\lambda = \sum \rho_i^{TOA} \cdot c_i + c_0 \tag{4}$$

where α_λ is the surface albedo for the spectral range of λ, ρ_i^{TOA} is the TOA reflectance for spectral band i, and c_i and c_0 are the regression coefficients.

To develop such a statistical relationship and apply the relationship to Landsat albedo estimation (Fig. 1), radiative transfer simulation was performed to simulate TOA reflectance by considering various types of surface, atmospheric, and geometric conditions. The sensor spectral response functions obtained from the USGS and the MODIS BRDF database were used as inputs to the vector version of the 6S radiative transfer code (Vermote et al., 1997) to simulate the TOA reflectance data. Detailed configurations of the simulations can be found in Table 4. Following the principle of generating global Landsat data products (Masek et al., 2006), continental aerosol was used as the default aerosol type in the radiative transfer simulation. Water vapor, ozone, and CO_2 settings are prescribed in the "US62" atmospheric profiles in 6S. An additional experiment was conducted to assess the improvements when using different aerosol types (e.g., desert, biomass burning, and urban aerosols) on albedo estimation at the SURFRAD sites. The linear regression coefficients in Eq. 4 for each of the geometrical combinations were pre-calculated and are stored in look-up tables (LUTs) for operational use. All the regression models in the LUT were estimated at the 99% confidence level.

Because of the data saturation problem over bright surfaces in TM and ETM + data, the visible bands do not always provide accurate

Table 4
Generic look-up table (LUT) configurations for simulating surface albedo and TOA reflectance data.

Parameters	Values
Solar zenith angle (°)	0, 5, 10, 15, 20, 25, 30, 35, 40, 45, 50, 55, 60, 65, and 70
View zenith angle (°)	0, 5, 10, 15, 20
Relative azimuth angle (°)	0, 30, 60, 90, 120, 150, and 180
Aerosol optical depth at 555 nm	0.05, 0.10, 0.15, 0.20, 0.30, 0.40, and 0.60

information. Thus, for albedo estimation over snow surfaces, we tested three sets of LUTs including one built by using all six Landsat spectral bands, hereafter referred to as SnowLUT1, and one built by using only the three infrared bands, which do not saturate, hereafter referred to as SnowLUT2. Both SnowLUT1 and SnowLUT2 are built up with the same geometric and atmospheric configurations as the generic LUT listed in Table 3. An additional LUT, SnowLUT3, was created on the basis of SnowLUT2 configurations with only lower aerosol loadings (0.05–0.20) used as inputs in the simulation. SnowLUT3 was used for particularly high latitude regions where the typical aerosol loading was lower than that over mid- to low-latitudes (von Hardenberg et al., 2012). Only the snow samples from the MODIS BRDF database were used in the radiative transfer simulations for the establishment of these three LUTs built up for snow surfaces. For visible bands with the saturation problem, TOA reflectance data were calculated directly by using the L1T digital numbers and conversion coefficients regardless of whether the data were saturated. For non-saturated data, the generic LUT was used regardless of whether the surface was covered by snow.

2.5. Temporal continuity of surface albedo from TM, ETM +, and OLI

To evaluate the temporal continuity of surface albedo estimated from Landsat series, an experiment was carried out to examine the difference of albedo estimates from different Landsat sensors during the overlapping periods. Because there is an 8-day acquisition difference between TM and ETM + and between ETM + and OLI, it is not possible to make direct albedo comparisons due to potential surface changes. To mitigate such effects on albedo intercomparison between different sensors, two efforts were made. First, albedo intercomparisons can be conducted at "pseudo" invariant sites where surface albedo did not
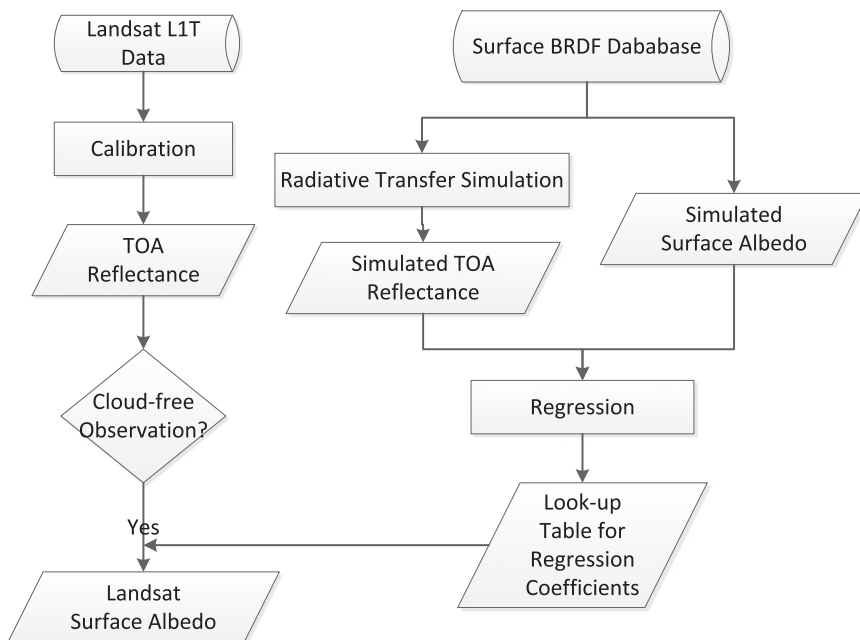
Fig. 1. Flowchart of albedo direct estimation from Landsat data. The surface BRDF database was built with the MODIS BRDF product. The 6S codes were used in the radiative transfer simulation.

have significant changes during the past three decades, at least in certain seasons. Among the sites listed in Table 3, three sites, including one desert site (DRA from SURFRAD), one vegetation site (GWN from SURFRAD), and one site with permanent snow (GVN from BSRN) were chosen. Second, monthly/seasonal averages of surface albedo were calculated from all the available clear-sky observations included in this study to remove the impacts of seasonal variation in surface albedo. Specifically, based on the Landsat data availability in this study only the data from September to October over DRA site, data from October to December over GWN site, and data from December to February for GVN site were included for intercomparison. To cross compare the temporal variation of satellite-derived albedo estimates, the ground measurements obtained at the same time of Landsat acquisition were also included, statistics of which were calculated in the same manner as those from the satellite-derived albedo estimates. Albedo anomalies from satellite estimates and ground measurements were calculated based on their respective mean values during the period of 1997–2016 to remove potential systematic bias between the datasets. The temporal continuity of Landsat albedo estimation was then examined through comparing the interannual variation of the time series albedo values derived from satellite estimates and ground measurements.

2.6. Inter-comparison between albedo estimates from MSS and TM data

Because the theoretical basis for the Landsat MSS sensor is the same as for the other three sensors, the question remains as to whether it is possible to generate surface albedo from MSS. Owing to the limited ground measurements available for matching the acquisition time with MSS before 1995, it is difficult to verify the MSS-derived surface albedo through direct comparison with ground measurements. Thus, it would be highly useful to conduct inter-comparisons of surface albedo estimates derived from MSS and other Landsat data to help verify the MSS albedo accuracy. To mitigate the acquisition time difference between MSS and other Landsat data to avoid differences in viewing geometries and atmospheric conditions, several pairs of MSS and TM images onboard the Landsat 5 satellite were chosen in this study for albedo estimation comparison.

Moreover, because the spatial resolution of the MSS image is twice that of the TM image, disregarding their point spread functions as well as their geolocation errors (Tucker et al., 2004) would increase the difference between their albedo values. To further investigate the impacts of point spread functions and geolocation errors, an analysis was conducted here based on inter-comparisons of MSS and TM albedo estimations at seven SURFRAD locations, covering a variety of land cover types (Table 5).

3. Results

3.1. Theoretical uncertainties in albedo estimation

Fitting RMSEs were used in this study to characterize the theoretical uncertainties of the direct estimation approach for each of the sensors in the estimation of surface albedo from the simulated data including

black-sky (BSA) and white-sky albedos (WSA) for broadband and spectral bands (Fig. 2). It is noteworthy that as a result of atmosphere-land surface interaction, the RMSEs shown here demonstrate the sensor's capability to estimate surface albedo from simulated TOA observations with reasonably small errors rather than that from surface directional reflectance. In general, spectral bands from the three types of sensors are able to estimate broadband albedos with similar accuracies, with RMSEs ranging from 0.01 to 0.03. The albedo estimation RMSE increased with the solar zenith angle for both spectral and broadband BSAs, likely as a result of the bowl shape of BSA dependence on the solar zenith angle (Yang et al., 2008). WSA estimation was similar to that of BSA except for the near-infrared bands. Among the four types of sensors, ETM + bands showed similar performance in the albedo estimation to TM bands. The OLI bands showed slight improvement in albedo estimation in both the visible and near-infrared spectral ranges as a result of the added band 1 (430–450 nm) for capturing aerosol information, which generated a magnitude of uncertainty in shortwave albedo estimation slightly better than that of TM and ETM +. In fact, the MSS data outperformed the other sensors in the estimation of visible and total shortwave albedo, which occurred likely because MSS bands have broader spectral coverage, and the errors in narrow-to-broadband conversion were mitigated. However, because MSS has only one band in the infrared spectral range the total near-infrared albedo accuracy was poorer than that from the other three sensors.

Besides the broadband albedos, the spectral albedo can also be generated by using data from other spectral bands with fitting RMSEs within 0.03 based on the simulated data. We determined that the uncertainty of spectral albedo estimation is related mainly to the band similarity of Landsat sensors to that of MODIS. For example, the significant decrease in uncertainty of ETM + band 5 (1.55–1.75 μm) is likely due to the shift in the band design in the shortwave-infrared range, resulting in improved correlation with MODIS bands.

3.2. Validation at SURFRAD sites

The validation of shortwave albedo against ground measurements showed promise at the SURFRAD sites (Fig. 3), with a small bias of approximately − 0.001 to − 0.011 and an RMSE of 0.028 to 0.030. Our results for snow-free cases show RMSEs from 0.023 to 0.027, which are close to those of 0.013–0.037 reported at the SURFRAD sites in Shuai et al. (2011). To overcome the saturation problem in TM and ETM + data, the snow albedo shown in Fig. 3 with a value larger than 0.4 was calculated by using SnowLUT2. The results generated from SnowLUT1 (not shown) have an overestimation of snow albedo up to ~0.05 compared with the results from SnowLUT2. Additional analysis through the use of the snow LUTs is provided in the validation at GC-Net sites where more snow albedo data are available.

The combined results from all three sensors on the albedo estimation ($N = 904$) showed a bias of − 0.007 with an RSME of 0.029 and R^2 of 0.925. The snow-free albedo estimation ($N = 865$) had a bias of − 0.008, RMSE of 0.026, and R^2 of 0.528, whereas the snow-covered cases ($N = 39$) had a bias of 0.007, RMSE of 0.067, and R^2 of 0.777.

Table 5
Location, time, and land cover information of MSS and TM data used for albedo comparison.

Site name	Scene no.	Date	Center Lat/Long (°N/°E)	Major land cover[a]
BON	p023r032	1991-04-01	40.3/− 98.1	Cropland, deciduous forest,
DRA	p040r035	1992-10-03	36.0/− 116.4	Shrubland, barren land
FPK	p035r026	1991-09-28	48.9/− 104.3	Cropland, grassland
GWN	p023r036	1991-08-23	34.6/− 90.5	Deciduous forest, cropland, wetland, grassland
PSU	p016r032	1992-05-20	40.3/− 78.0	Deciduous forest, grassland, cropland
SXF	p029r030	1988-06-21	43.2/− 97.1	Cropland, grassland
TBL	p034r032	1992-06-19	40.3/− 105.8	Evergreen forest, shrubland, grassland

[a] Major land cover information is obtained from the National Land Cover Database 2006 (NLCD2006) (Fry et al., 2011).
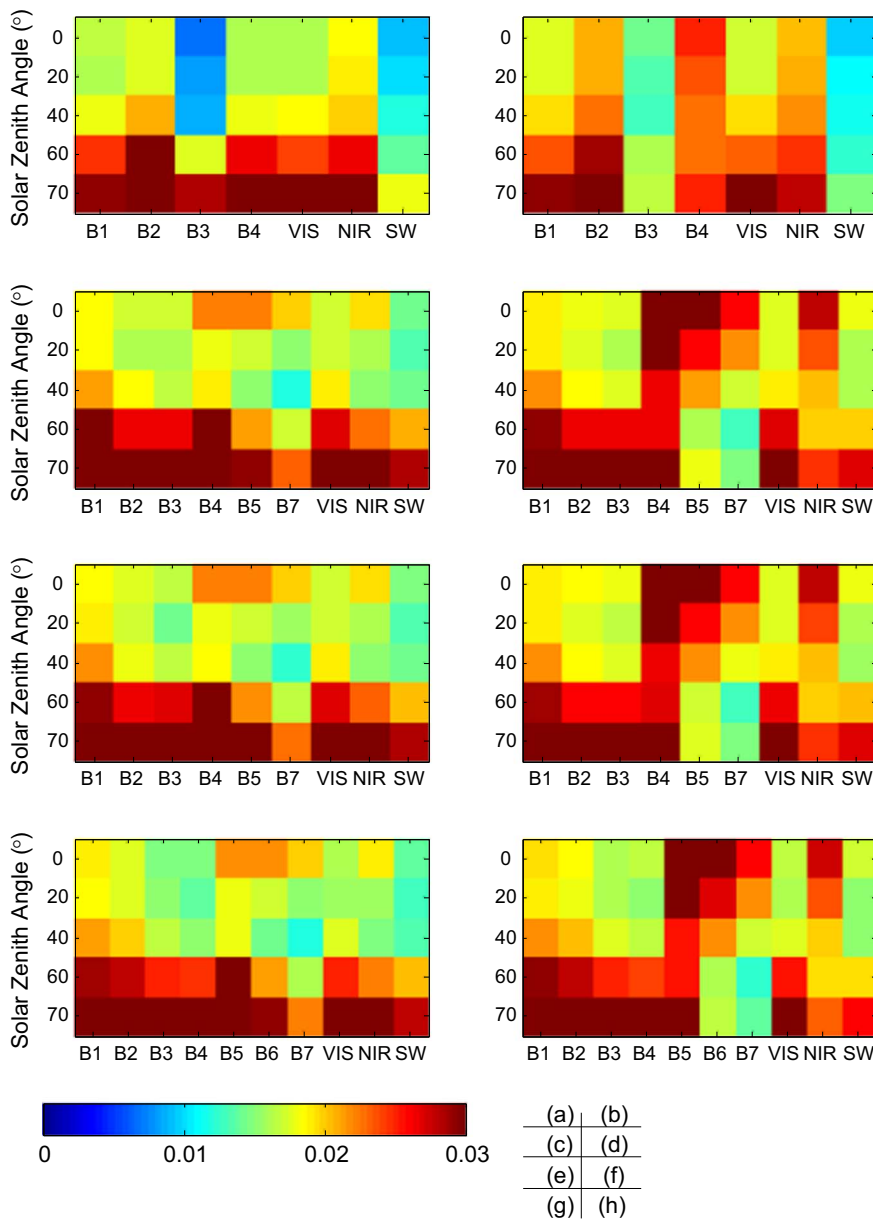
Fig. 2. RMSEs of surface albedo estimation from simulated Landsat data: (a) MSS BSA; (b) MSS WSA; (c) TM BSA; (d) TM WSA; (e) ETM + BSA; (f) ETM + WSA; (g) OLI BSA; and (h) OLI WSA. X-axis stands for the spectral bands and three broadbands including visible (VIS: 300–700 nm), near-infrared (NIR: 700–3000 nm), and shortwave (SW: 300–3000 nm).

The results also show that our algorithms had similar performance for the data from the three sensors, among which the results from OLI were slightly better in terms of bias and R^2. This might be attributed to its improved signal-to-noise ratio (SNR) and radiometric quantization compared with TM and ETM +.

At the Desert Rock (DRA) site, surface albedo has been consistently overestimated compared with ground measurements for all three sensors. For example, validation of albedo estimated from the TM data showed a bias of 0.021 and an RMSE of 0.022, which indicates that the estimation bias is the primary factor contributed to the uncertainty. The default "continental" aerosol type used in this study likely led to the overestimation. An additional experiment was conducted by changing the aerosol type to "desert", which greatly improved the albedo estimation by reducing the bias and RMSE to 0.010 and 0.012, respectively. Because the land surface at the DRA site is relatively stable with the least amount of cloud cover among all SURFRAD sites, data from this site are helpful for evaluating the stability of the direct estimation algorithm. Calculated from the clear-sky Landsat TM observations and ground measurements during 1998–2011, our retrievals showed very stable albedo estimates with an average value of 0.213 ± 0.007; the

ground measurements during this period had an average value of 0.203 ± 0.008.

For the other SURFRAD sites, by changing the default "continental" aerosol to "biomass burning" and "urban" aerosols, albedo estimation accuracy changes from site to site with an RMSE difference of < 0.004. This suggests that with an accurate aerosol type map, albedo estimation may improve a little for non-desert area, which confirms the finding in our earlier study (Liang, 2003).

3.3. Validation at AmeriFlux sites

The validation results for snow-free cases over AmeriFlux sites showed a similar estimation accuracy of shortwave albedo to that over SURFRAD sites (Fig. 4). However, for snow-covered cases, the results were slightly worse with an overestimation of approximately 0.05 (not shown). The overall estimation accuracy for shortwave albedo over snow-free ($N = 662$) cases for TM data was reasonable with an RMSE and R^2 of 0.026 and 0.587, respectively. Results from ETM + data ($N = 625$) showed very similar accuracy of albedo estimation with an RMSE of 0.026 and an R^2 of 0.561. The shortwave albedo accuracy over
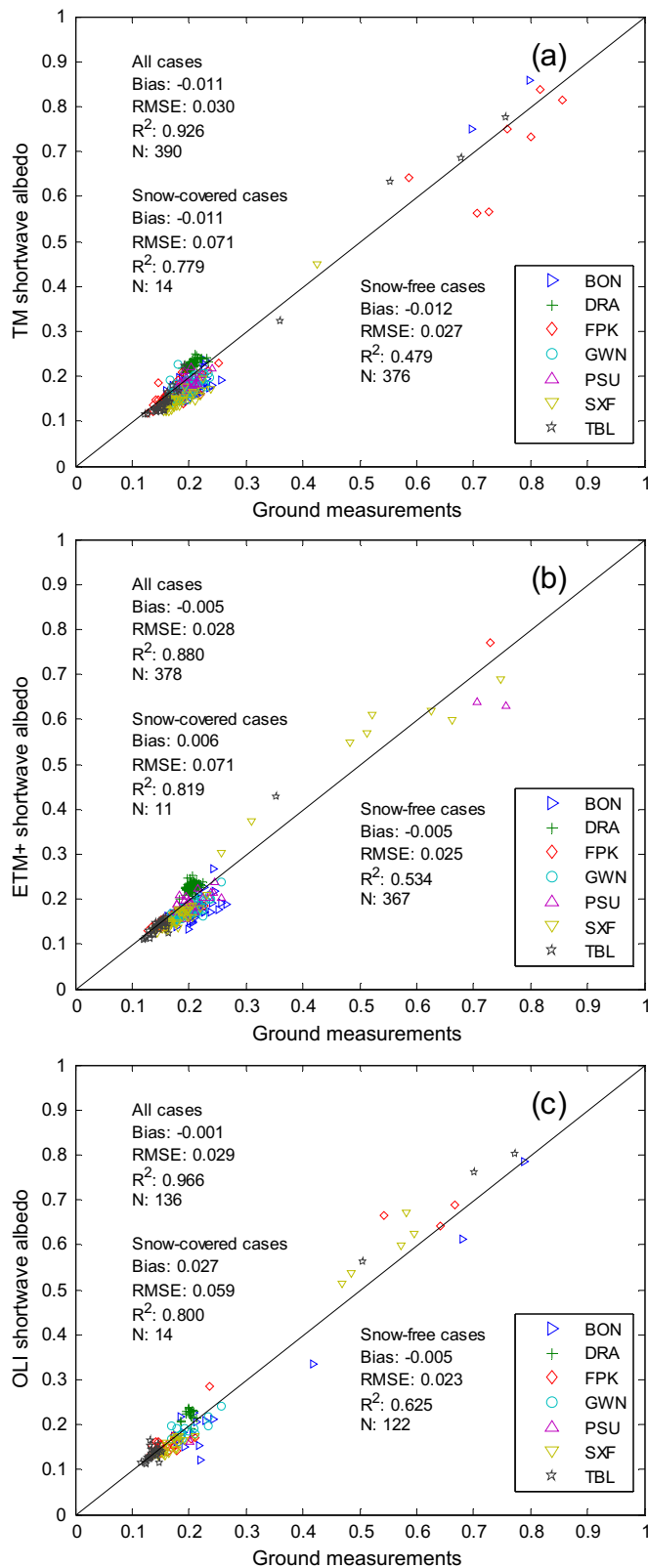
Fig. 3. Intercomparison of shortwave albedo and ground measurements at SURFRAD sites: (a) Landsat 5 TM; (b) Landsat 7 ETM +; and (c) Landsat 8 OLI.

AmeriFlux sites was slightly worse than that at SURFRAD sites possibly due to the reduced data quality of ground measurements.

By using the radiation data available at the visible spectral range, we investigated the visible albedo estimation from Landsat data. Such an investigation has not been reported previously against ground

measurements. In Fig. 4, the estimation of visible albedo shows a similar error magnitude to that of shortwave albedo, with RMSEs of 0.026 and 0.027 for TM and ETM +, respectively. Moreover, visible albedo estimation always showed a higher R^2, at 0.668 for TM and 0.647 for ETM +, than that of shortwave albedo estimation at 0.587 for TM and 0.561 for ETM +. This result occurred likely because aerosol scattering is the main atmospheric factor influencing visible radiation, whereas the water vapor content also affects shortwave radiation in ground measurements. Thus, inclusion of a correction for the water vapor content may help further improve the shortwave albedo estimation. It is noteworthy the spectral coverage difference between the retrieved visible albedo (300–700 nm) and the AmeriFlux observations (400–700 nm). According to the surface reflectance spectra database, the integrated broadband reflectance values for 300–700 nm have an underestimation of 0.008 compared with the data for 400–700 nm over non-snow surfaces, which likely explains the majority of negative bias shown in Fig. 4b and d.

Again, the visible albedo estimation exhibited an overestimation over snow-covered surfaces. Nevertheless, the snow-covered samples were very limited, making it difficult to reach solid conclusions on the algorithm's performance over snow cases at the mid- to low-latitude sites. Further discussion for snow-covered cases is provided in the validation of GC-Net sites.

The accuracy of surface albedo estimation showed a dependence on land cover type. AmeriFlux sites cover multiple land cover types and were thus used for accuracy assessment. We separated the sites according to land cover type and calculated the estimation accuracy of corresponding TM-based snow-free albedo for each land cover type (Table 6). In general, the absolute albedo accuracy was better for densely vegetated forest sites with lower albedo values than that for sparsely vegetated cropland and grassland sites with higher albedo values. However, the albedo estimation for evergreen needle leaf forest presented a larger uncertainty among all land cover types with the largest standard deviation of its albedo values occurring in both shortwave and visible spectral ranges. Unlike deciduous broadleaf forest (DBF), viewing geometry differences from the nadir-view Landsat sensor and the hemispherical-view ground instrument likely led to the larger albedo variation at 30-m scales and hence the albedo estimation uncertainty at evergreen needleleaf forest (ENF) sites. Albedo estimates at the ENF sites were separated into three groups according to their solar zenith angles θ_s: $\theta_s \le 40°$, $40° < \theta_s \le 60°$, and $\theta_s > 60°$. The albedo estimation RMSEs for the three groups were 0.019, 0.024, and 0.054, respectively, which increased with an increase in solar zenith angle. This occurred because that nadir-view satellite sensor can see deeper through the canopy, whereas the pyranometer, with a wide field-of-view also receives reflected energy from the ground whether sunlit or in shadow. With a change in the solar zenith angle, changes between that viewed by the satellite and the pyranometer greatly affect the data comparison, which is particularly important when there was partial snow cover at the ENF sites. To further exclude data with partial snow-cover, the normalized difference snow index (NDSI) was used. Table 6 shows that for the ENF samples with NDSI < 0.4 albedo estimation accuracy is generally comparable to that at DBF sites. Among all land cover types, lower R^2 values were observed for albedo estimation at CRO and GRA sites; however, this is not well-understood. One possible explanation is that because the pyranometers for the CRO and GRA sites are usually 3 m to 6 m above the surface, reflection from the instruments and the limited spatial representativeness of the flux measurements may contribute to the estimation uncertainty.

The spatial representation of ground measurements has been identified in MODIS albedo validation (Roman et al., 2013). To help the investigation of whether the quality of ground measurements or spatial representation led to albedo estimation uncertainty, nine AmeriFlux sites identified as non-homogeneous sites at the MODIS resolution (Wang et al., 2015) were selected to evaluate the accuracy of the Landsat albedo estimation. In fact, over such non-homogeneous sites,
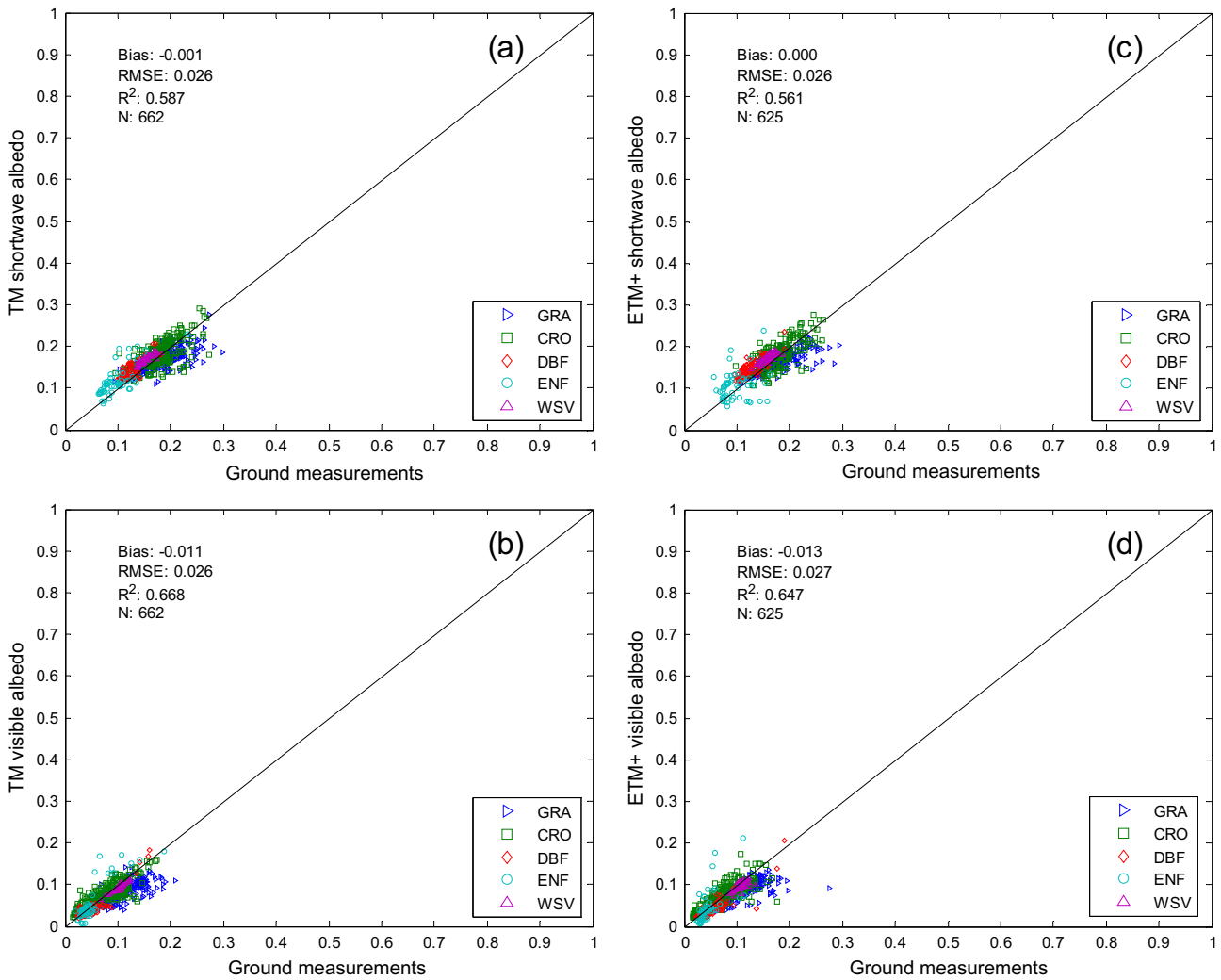
Fig. 4. Intercomparison of Landsat albedo and ground measurements at AmeriFlux sites: (a) TM shortwave albedo; (b) TM visible albedo; (c) ETM + shortwave albedo; and (d) ETM + visible albedo. Colors represent different land cover types. (For interpretation of the references to color in this figure legend, the reader is referred to the web version of this article.)

Table 6
Albedo estimation accuracy for various land cover types.

Broadband albedo	Land cover type	N	Mean	SD	Bias	RMSE	R²
Shortwave	CRO	228	0.182	0.030	0.002	0.027	0.401
	GRA	255	0.167	0.024	−0.015	0.028	0.544
	WSV	53	0.168	0.010	0.014	0.015	0.807
	DBF	67	0.145	0.022	0.018	0.022	0.649
	ENF (all samples)	59	0.117	0.035	0.019	0.030	0.563
	ENF (NDSI < 0.4)	51	0.106	0.021	0.015	0.024	0.310
Visible	CRO	228	0.074	0.030	−0.001	0.020	0.705
	GRA	255	0.083	0.025	−0.026	0.034	0.603
	WSV	53	0.092	0.010	−0.010	0.011	0.854
	DBF	67	0.045	0.031	−0.006	0.014	0.820
	ENF (all samples)	59	0.053	0.044	0.004	0.023	0.751
	ENF (NDSI < 0.4)	51	0.037	0.018	−0.002	0.013	0.494

SD: standard deviation; NDSI: normalized difference snow index.

Fig. 5 shows that our Landsat albedo estimation achieved accuracy similar to that using all of the AmeriFlux sites listed in Table 3. Therefore, our albedo estimation over those sites can be used as a reference for validating coarse-resolution data to bridge the scale gaps.

3.4. Validation at BSRN sites

Similar to the data collection and processing procedure used for data from SURFRAD sites, surface shortwave albedo estimated from TM and ETM + were generated and compared with ground measurements obtained globally from BSRN sites. These sites also encompass a variety of land cover types and climate regions. The TM and ETM + results were generally comparable, with RMSEs between 0.022 and 0.029 and R² values between 0.974 and 0.991, respectively, including both snow-free and snow-covered cases (Fig. 6). Combining the results from TM and ETM +, the albedo estimation showed a bias of − 0.012, RMSE of 0.022, and R² of 0.635 (N = 230) for snow-free cases, and a bias of − 0.010, RMSE of 0.040, and R² of 0.828 (N = 54) for snow-covered cases. This estimation accuracy is similar to that shown at SURFRAD and AmeriFlux sites, which suggests that this unified algorithm does not cause significant errors at various seasons and locations. It should be noted is that our results of snow-covered shortwave albedos, including the results at SURFRAD sites, have proven to be accurate over various non-permanent snow/ice land cover types compared with the accuracy of the Landsat 8 OLI-based albedo recently reported in Wang et al. (2016).

3.5. Validation at GC-Net sites

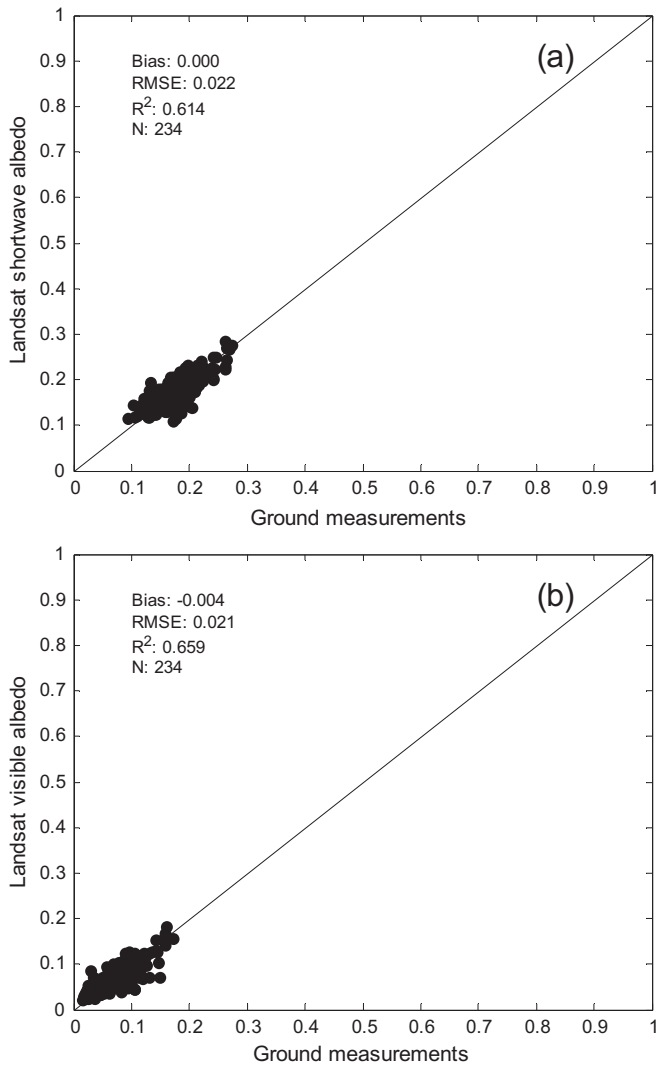Ground measurements and ETM + data collected at four GC-Net

Fig. 5. Intercomparison of Landsat TM albedo and ground measurements at selected non-homogeneous AmeriFlux sites: (a) shortwave albedo; and (b) visible albedo.

Fig. 6. Validations results of albedo estimation at BSRN sites from (a) ETM +; and (b) TM.

Table 7
Comparison of Landsat albedo estimates from using different LUTs and ground measurements at GC-Net sites (sample size is 73).

	SnowLUT1	SnowLUT2	SnowLUT3
Bias	0.022	− 0.001	− 0.024
RMSE	0.044	0.031	0.039
R^2	0.609	0.786	0.751

sites were used in the comparison to test the direct estimation algorithm over bright surfaces (Table 7). Although Landsat data showed saturation problem over snow surfaces, the comparison results from SnowLUT1 based on all six spectral bands had an overestimation compared with ground measurements with a bias of 0.022, RMSE of 0.044, and uncertainty of about 5% in terms of the relative accuracy. The pyranometer of GC-Net sites measures only part of the total shortwave spectral domain, at 400–1100 nm, and the Landsat albedos were retrieved for $300 - 3000$ nm. Therefore, an average overestimation in albedo values of about 0.035 was reported at GC-Net sites for ground measurements at 400–1100 nm compared with the values at $300 - 3000$ nm (Stroeve et al., 2013; Stroeve et al., 2006). Thus, the results from SnowLUT1 would always overestimate shortwave surface albedo. After excluding the data from the visible bands, the albedo estimation from SnowLUT2 improved significantly with a smaller bias of − 0.001 and an R^2 close to 0.8. Moreover, the relative uncertainty dropped to ∼4%. However, the results from SnowLUT2 still showed some overestimation if the systematic measurement bias was considered. Given the fact that the aerosol loadings over polar regions are significantly lower than those at mid- to low-latitudes (von Hardenberg et al., 2012), further investigation showed that if only the low-aerosol loadings at 0.05 to 0.20 (Liang et al., 2005), were considered in building the LUT with near-infrared bands (SnowLUT3) our Landsat retrievals were closer to the actual albedo. The negative bias of 0.024
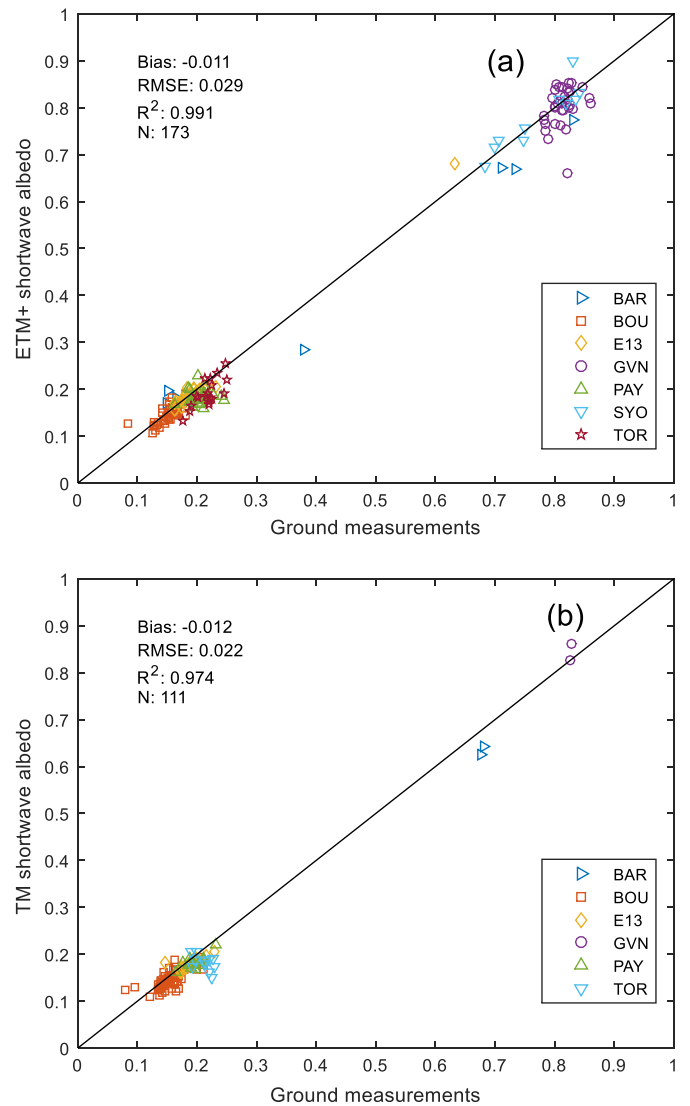
from SnowLUT3 results is closer to the value of 0.035 reported in previous studies (Stroeve et al., 2013; Stroeve et al., 2006).

Owing to the difference in spectral coverage between ground measurements and Landsat albedo retrievals, it is difficult to investigate the actual bias of the Landsat albedo estimation approach. Thus, the MODIS albedo product was introduced here to help verify the Landsat albedo retrievals. The results shown in Fig. 7 suggest that these two datasets have a very good agreement with an RMSE of 0.031 and R^2 of 0.943, whereas the Landsat albedo values have a very slight bias of 0.007 compared with the MODIS data. Because only the best quality MODIS albedo retrievals were selected as shown in Fig. 7, the sample size ($N = 48$) is smaller than that in Table 7 ($N = 73$). If all of the Landsat retrievals were included in the comparison with MODIS data and the
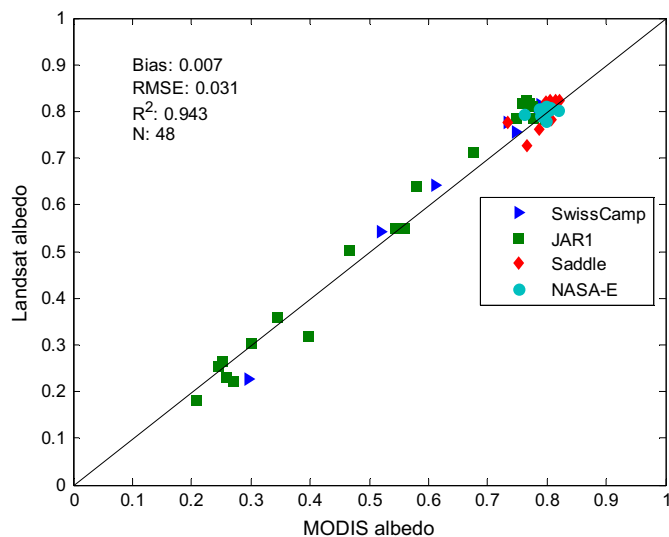
Fig. 7. Comparison of surface albedo derived from Landsat ETM + and best quality (quality flag equals to zero) MODIS albedo product (MCD43A3) at GC-Net sites.

data availability of ground measurements was not considered, the comparison results were slightly worse with a bias of 0.010 and am RMSE of 0.037 (N = 645); R^2 decreased significantly owing to the clustered high albedo values within the range of 0.7–0.9. This suggests that the Landsat albedo estimation approach adopted in this study, SnowLUT3, did not lead to significant bias in the shortwave albedo with the MODIS albedo products used as a reference.

3.6. Preliminary assessment of temporal continuity of albedos from TM, ETM +, and OLI

Based on the simplified method proposed in Section 2.5, the temporal continuity was tested with interannual values of monthly/seasonal averages of surface albedo estimates from TM, ETM +, and OLI at DRA, GWN, and GVN sites. Time series of surface albedos from Landsat and ground measurements were shown in Fig. 8, in which different colors represent data from different sensors. During the overlapping period with data from two sensors, the albedo values from ground measurements were calculated based on the satellites' actual acquisition date and time so that two values might be plotted for the same year due to the acquisition time differences. It should be also noted that for some year the data point was not shown because either clear-sky satellite observations or ground measurements were not available.

At the desert site (DRA), the temporal variation of the ground measurements during the period of 1998–2015 was around ± 0.005 (1σ). The albedo anomalies derived from the Landsat estimates and ground measurements had an overall negligible difference of 0.000 ± 0.005 for the whole period. This suggests that the Landsat estimates captured the interannual variation in surface albedo quite well although a consistent overestimation of about 0.018 was observed due to the use of the generic LUT (discussed in Section 3.2). In the 11-year overlapping period of TM and ETM +, there was a slight overestimation of ETM + albedo than TM albedo by 0.003 ± 0.005, while the difference calculated in the same way but using ground measurements was 0.001 ± 0.002. In the 3-year overlapping period of ETM + and OLI, the overall bias between albedo anomalies from the two sensors was very small with a slight overestimation of 0.003 from ETM + albedos over OLI estimates.

Compared to the desert site, the vegetation site and snow site observed more interannual variations in surface albedo even after the seasonal variation was considered. At the vegetated site (GWN), Landsat surface albedo estimation had a general underestimation around 0.02 as shown in Fig. 3 and Fig. 8. The interannual variation in
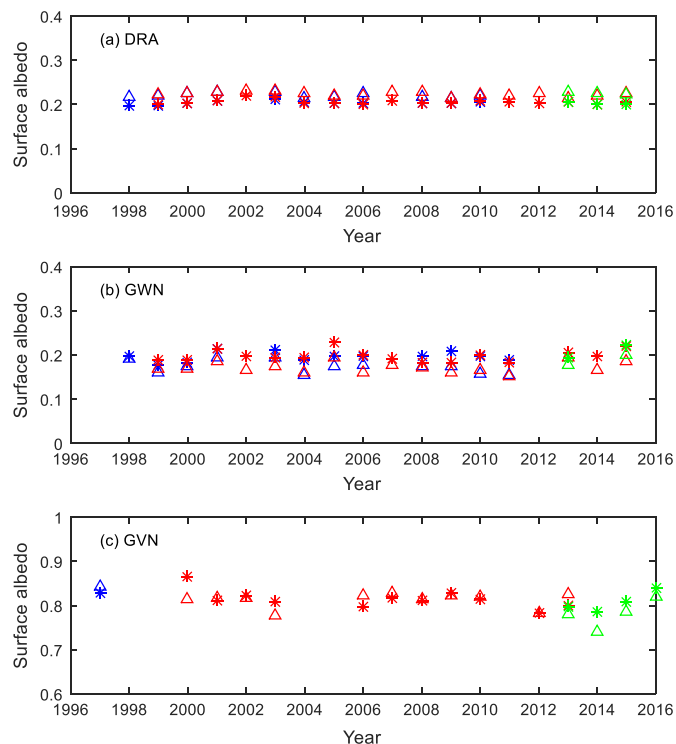

Fig. 8. Albedo time series from ground measurements and Landsat estimates: (a) DRA site (September to October); (b) GWN site (October to December); and (c) GVN site (December to February). Stars represent ground measurements and triangles represent Landsat estimates. Albedos from TM, ETM +, and OLI are in blue, red, and green, respectively. (For interpretation of the references to color in this figure legend, the reader is referred to the web version of this article.)

surface albedo ground measurements was around ± 0.013 (1σ). The albedo anomalies from the Landsat data matched well with those from the ground measurements with a difference of 0.000 ± 0.009. Again, there was an overestimation of 0.002 ± 0.012 from the ETM + albedo estimates compared with TM values from 1999 to 2011, while in the same period there was no significant difference (0.000 ± 0.015) from the ground measurements. Similar to the results at DRA site, the ETM + estimates had an overestimation of 0.003 than the albedo values from the OLI data during 2013–2015, in which period the difference derived from ground measurements was around 0.001.

At both DRA and GWN sites, ETM + albedos had a small overestimation (0.002–0.003) compared to TM and OLI values. This can be partly explained by the difference in the way for calculating the average values, in which ETM + observations were found to have larger solar zenith angles in general.

Unlike the above two sites, not enough data within the overlapping periods of two sensors can support the same statistical intercomparison at the GVN site, which was covered by permanent snow in the Antarctica. The interannual albedo variation during 1997–2016 was around ± 0.021 (1σ) with an average value of 0.814. The Landsat estimates combining data from three sensors had a small negative bias of 0.007 compared to ground measurements. The Landsat albedo anomalies matched with the values from ground measurements quite well with a difference of 0.000 ± 0.023, which was a combined result of overestimations found in the albedos from the earlier sensors (0.022 for TM and 0.005 for ETM +) and an underestimation of 0.020 in OLI albedo estimation. Although the ETM + albedo estimates were consistent with the ground measurements during the period of 2000–2013, more data from TM and OLI are expected to provide a more reliable assessment of temporal continuity of albedo estimation at this site.
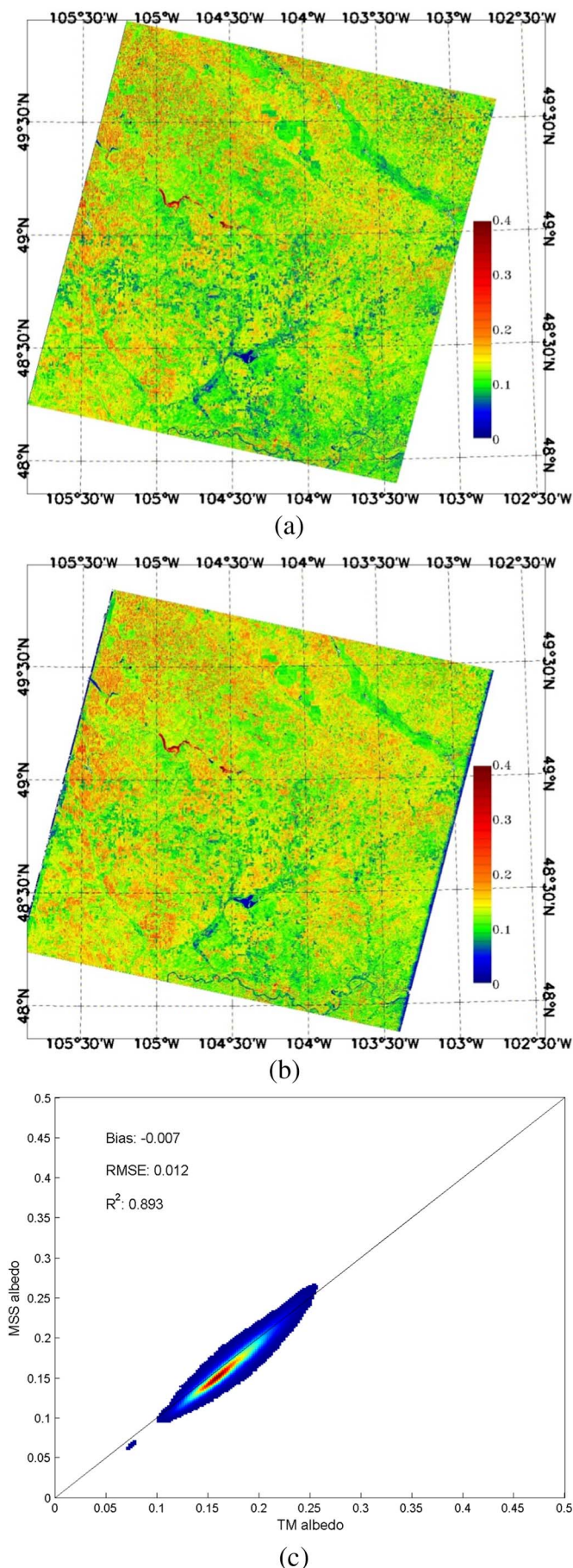
(a)

(b)

(c)

Fig. 9. Comparison of shortwave black-sky albedo estimates from (a) MSS data; and (b) TM data onboard Landsat 5. (c) Scatterplot and statistics; the density plot uses color from blue to red to represent density from low to high. The data were acquired on September 28th, 1991 (p035r026). (For interpretation of the references to color in this figure legend, the reader is referred to the web version of this article.)

3.7. Possibility for generating surface albedo from MSS data

Fig. 9 shows an example of the albedo maps derived from MSS and aggregated TM data. These values generally agreed very well in terms of both spatial distribution and absolute difference in magnitude with an RMSE of 0.012 and an R^2 of 0.893. A slight negative bias of 0.007 between MSS and TM albedo values can be attributed to the errors in sensor calibration and band conversion.

Visual investigation revealed that the relative geolocation errors between MSS and TM onboard Landsat 5 were as large as two MSS pixels (~120 m). In addition, a lower SNR of MSS and point spread function differences between the two sensors together led to reduced radiometric separability of MSS data compared with that of TM data even when the latter was aggregated with 60 m. To investigate the impact of these issues in the accuracy assessment, a subset of the Landsat image pair over flat terrain was extracted, as shown in Fig. 10. The albedo spatial patterns from the two sensors generally agreed well. The difference map showed that large differences up to ± 0.05 existed at the boundary between high- and low-albedo areas, as represented by red and purple colors in Fig. 10c. On the contrary, the differences were relatively stable in the upper right corner of the subset where the surface type is homogenous, which represents the bias between the two albedo datasets. This result demonstrates that the relative geolocation errors in MSS data can contribute greatly to the RMSE in such as inter-comparison shown in Fig. 9.

Statistics of inter-comparisons made with MSS and TM data pairs are tabulated in Table 8, which shows good agreement between albedo estimates from MSS and TM data with RMSEs of 0.011 to 0.017 and R^2s of 0.858 to 0.963 over a variety of land cover types. An exception is the SXF case, in which geolocation errors caused by abundant rugged terrain in the scene led to albedo differences. Moreover, the smaller range of albedo values also contributed to the low R^2 found for the SXF case; in such a case, spatial aggregation of the comparison to 480 m can greatly improve the results, with an RMSE of 0.012 and R^2 of 0.756. Additional research is needed to understand the albedo difference caused by sensor calibration and the geolocation accuracy of the two datasets.

4. Discussion and conclusions

Satellite albedo products at fine resolution allow for applications such as agricultural monitoring, urban environment assessment, and forest management; therefore, the demand for these products is increasing. Moreover, such products are crucial for validating coarse-resolution satellite products and reanalysis data, the accuracy of which is often difficult to evaluate with point-based ground measurements, particularly over heterogeneous landscapes. In this study, we adopted a refined direct estimation algorithm and applied it to multiple Landsat satellite sensors with the possibility of producing surface albedo estimates dating back to the 1980s.

The direct estimation approach has unique advantages over traditional albedo algorithms for fine-resolution satellite data with low revisit frequency. First, its retrieval rate is higher than that obtained by using the traditional method because it does not sample the surface anisotropy. Second, there is no need for concurrent coarse-resolution data or ancillary data as inputs. Third, it can generate surface albedo over both snow-free and snow-covered surfaces. Finally, it can be easily extended to other fine-resolution data similar to Landsat data (e.g., Sentinel-2).

Extensive validation made against ground measurements show that
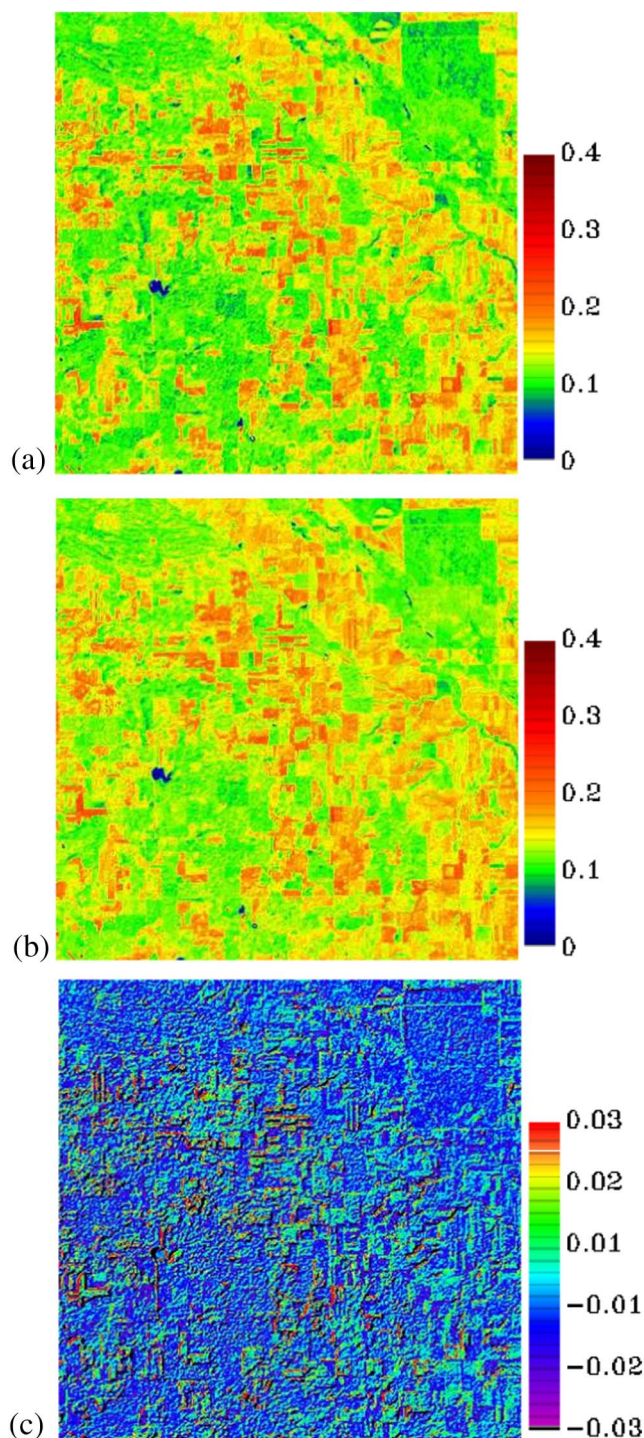
Fig. 10. Subsets (2.4 km × 2.4 km) of shortwave black-sky albedo estimates from (a) MSS data; and (b) TM data as shown in Fig. 9. (c) Difference map between (a) and (b). (For interpretation of the references to color in this figure, the reader is referred to the web version of this article.)

the proposed approach can generate reliable surface albedo estimates with accuracy of 0.022 to 0.034 in terms of RMSEs over snow-free surfaces. These results are comparable to those reported in previous studies (Franch et al., 2014; Shuai et al., 2011; Shuai et al., 2014). For snow-covered surfaces, the validations at GC-Net sites showed a significant improvement in albedo estimation accuracy with RMSEs of about half those reported in previous results that used MODIS data. This highlights the utility of fine-resolution albedo data in calibrating coarse-resolution data for cryosphere applications.

Table 8
Statistics of intercomparison of shortwave albedo estimates from Landsat 5 TM and MSS data over different locations (statistics are calculated at the 99% confidence level).

Site name	Mean	SD[a]	Bias[b]	RMSE	R^2	Samples
BON	0.169	0.027	− 0.006	0.013	0.872	9,095,158
DRA	0.212	0.056	0.001	0.012	0.963	9,119,333
FPK	0.171	0.029	− 0.007	0.012	0.893	9,379,374
GWN	0.163	0.033	0.007	0.015	0.910	8,945,138
PSU	0.159	0.022	0.005	0.011	0.858	9,122,343
SXF	0.151	0.021	0.003	0.018	0.582	9,095,044
TBL	0.142	0.060	0.004	0.017	0.925	9,057,375

[a] Mean and standard deviation (SD) are calculated from the TM albedo values.
[b] Bias is the mean value of MSS albedo data minus TM albedo data.

By comparing the albedos estimated from TM, ETM +, and OLI data, a generally good temporal continuity has been demonstrated over different land covers (desert, vegetation, and snow) through a period of more than two decades. The difference in them is within the error range of spectral band conversion and sensor calibration in addition to the acquisition time difference. According to this preliminary assessment, temporal continuity of surface albedo from Landsat satellite series can be achieved with a difference up to 0.003 using the unified estimation approach in this study. More work is expected to investigate the temporal continuity issue more extensively.

Good agreement was reached between albedo estimates from MSS and TM data with RMSE of 0.011 to 0.018 and R^2 of 0.582 to 0.963, which shows the possibility for further extension of the albedo data record to the pre-TM era. However, the actual albedo data quality also depends on radiometric and geometric calibration accuracy for the MSS data. Further efforts are needed to evaluate the long-term consistency of MSS-derived surface albedo, particularly during the pre-TM era.

Applying the empirical method may introduce errors in certain regions (e.g. desert) if a proper aerosol type is not used. Although the default continental aerosol type generally applies to most locations without introducing significant bias, our experiment shows that it is possible to improve the estimation by incorporating a location-based aerosol type map into the retrieval procedure. Inclusion of a land cover type-based LUT may further improve the estimation accuracy (Wang et al., 2013).

Another possible limitation of the current approach is associated with the imperfect strategy for building the BRDF database. In particular, owing to the strategy adopted here for collecting the BRDF samples from the MODIS products only high quality data over homogeneous areas were included. Thus, it is possible that BRDF shapes from partial snow-covered vegetation surfaces are underrepresented in the derived LUTs, hence increasing uncertainties in the albedo estimation for vegetation surfaces partially covered by snow. However, only very limited number of albedo ground measurements over such land surfaces were available to match the cloud-free Landsat scenes in validations. As a result, further effort is needed to improve the albedo estimation over partial snow-covered vegetation surfaces by incorporating more ground measurements and high quality BRDF samples.

Over mid- to high-latitude regions, Landsat TM and ETM + showed saturation problems in the visible bands over snow surfaces. In those cases, our approach of using the non-saturated bands showed better results than those obtained when all spectral bands were used. To further improve the results, particularly for ETM + data, the panchromatic band can be included in the retrieval procedure. In addition, for observations under large solar zenith angles > 65°, incorporating the in-situ surface BRDF measurements for snow and ice in radiative transfer simulations may also help reduce the estimation uncertainty. Topography correction, an additional parameter for improvement, will be covered in future research.

Acknowledgments

References

Baldridge, A.M., Hook, S.J., Grove, C.I., Rivera, G., 2009. The ASTER spectral library version 2.0. Remote Sens. Environ. 113, 711–715.

Burakowski, E.A., Ollinger, S.V., Lepine, L., Schaaf, C.B., Wang, Z., Dibb, J.E., Hollinger, D.Y., Kim, J.H., Erb, A., Martin, M., 2015. Spatial scaling of reflectance and surface albedo over a mixed-use, temperate forest landscape during snow-covered periods. Remote Sens. Environ. 158, 465–477.

Chander, G., Markham, B.L., Helder, D.L., 2009. Summary of current radiometric calibration coefficients for Landsat MSS, TM, ETM +, and EO-1 ALI sensors. Remote Sens. Environ. 113, 893–903.

Clark, R.N., Swayze, G.A., Wise, R., Livo, E., Hoefen, T., Kokaly, R., Sutley, S.J., 2007. USGS Digital Spectral Library splib06a. U.S. Geological Survey, Digital Data Series 231.

Franch, B., Vermote, E.F., Claverie, M., 2014. Intercomparison of Landsat albedo retrieval techniques and evaluation against in situ measurements across the US SURFRAD network. Remote Sens. Environ. 152, 627–637.

Fry, J.A., Xian, G., Jin, S.M., Dewitz, J.A., Homer, C.G., Yang, L.M., Barnes, C.A., Herold, N.D., Wickham, J.D., 2011. Completion of the 2006 National Land Cover Database for the conterminous United States. Photogramm. Eng. Remote. Sens. 77, 858–864.

Gao, F., He, T., Masek, J.G., Shuai, Y.M., Schaaf, C.B., Wang, Z.S., 2014. Angular effects and correction for medium resolution sensors to support crop monitoring. IEEE J. Sel. Top. Appl. Earth Obs. Remote. Sens. 7, 4480–4489.

Ghimire, B., Williams, C.A., Masek, J., Gao, F., Wang, Z., Schaaf, C., He, T., 2014. Global albedo change and radiative cooling from anthropogenic land cover change, 1700 to 2005 based on MODIS, land use harmonization, radiative kernels, and reanalysis. Geophys. Res. Lett. 41, 9087–9096.

von Hardenberg, J., Vozella, L., Tomasi, C., Vitale, V., Lupi, A., Mazzola, M., van Noije, T.P.C., Strunk, A., Provenzale, A., 2012. Aerosol optical depth over the Arctic: a comparison of ECHAM-HAM and TM5 with ground-based, satellite and reanalysis data. Atmos. Chem. Phys. 12, 6953–6967.

He, T., Liang, S.L., Wang, D., Wu, H., Yu, Y., Wang, J., 2012. Estimation of surface albedo and directional reflectance from Moderate Resolution Imaging Spectroradiometer (MODIS) observations. Remote Sens. Environ. 119, 286–300.

He, T., Liang, S.L., Song, D.X., 2014a. Analysis of global land surface albedo climatology and spatial-temporal variation during 1981–2010 from multiple satellite products. J. Geophys. Res. Atmos. 119, 10281–10298.

He, T., Liang, S.L., Wang, D., Shuai, Y., Yu, Y., 2014b. Fusion of satellite land surface albedo products across scales using a multiresolution tree method in the north central United States. IEEE Trans. Geosci. Remote Sens. 52, 3428–3439.

He, T., Liang, S.L., Wang, D., Chen, X., Song, D.X., Jiang, B., 2015a. Land surface shortwave albedo from Chinese HJ satellites based on a direct estimation approach. Remote Sens. 7, 5495–5510.

He, T., Liang, S.L., Wang, D.D., Shi, Q.Q., Goulden, M.L., 2015b. Estimation of high-resolution land surface net shortwave radiation from AVIRIS data: algorithm development and preliminary results. Remote Sens. Environ. 167, 20–30.

Ju, J.C., Roy, D.P., Vermote, E., Masek, J., Kovalskyy, V., 2012. Continental-scale validation of MODIS-based and LEDAPS Landsat ETM plus atmospheric correction methods. Remote Sens. Environ. 122, 175–184.

Karnieli, A., Ben-Dor, E., Bayarjargal, Y., Lugasi, R., 2004. Radiometric saturation of Landsat-7 ETM + data over the Negev Desert (Israel): problems and solutions. Int. J. Appl. Earth Obs. Geoinf. 5, 219–237.

Kim, W., He, T., Wang, D.D., Cao, C.Y., Liang, S.L., 2014. Assessment of long-term sensor radiometric degradation using time series analysis. IEEE Trans. Geosci. Remote Sens. 52, 2960–2976.

Kuusinen, N., Tomppo, E., Shuai, Y., Berninger, F., 2014. Effects of forest age on albedo in boreal forests estimated from MODIS and Landsat albedo retrievals. Remote Sens. Environ. 145, 145–153.

Lagomasino, D., Price, R.M., Whitman, D., Melesse, A., Oberbauer, S.F., 2015. Spatial and temporal variability in spectral-based surface energy evapotranspiration measured from Landsat 5TM across two mangrove ecotones. Agric. For. Meteorol. 213, 304–316.

Li, W.J., Fang, H.L., 2015. Estimation of direct, diffuse, and total FPARs from Landsat

surface reflectance data and ground-based estimates over six FLUXNET sites. J. Geophys. Res. Biogeosci. 120, 96–112.

Li, Z.Q., Garand, L., 1994. Estimation of surface albedo from space - a parameterization for global application. J. Geophys. Res.-Atmos. 99, 8335–8350.

Liang, S.L., 2003. A direct algorithm for estimating land surface broadband albedos from MODIS imagery. IEEE Trans. Geosci. Remote Sens. 41, 136–145.

Liang, S.L., Strahler, A.H., Walthall, C., 1999. Retrieval of land surface albedo from satellite observations: a simulation study. J. Appl. Meteorol. 38, 712–725.

Liang, S.L., Fang, H.L., Kaul, M., Van Niel, T.G., McVicar, T.R., Pearlman, J.S., Walthall, C.L., Daughtry, C.S.T., Huemmrich, K.F., 2003. Estimation and validation of land surface broadband albedos and leaf area index from EO-1 ALI data. IEEE Trans. Geosci. Remote Sens. 41, 1260–1267.

Liang, S.L., Stroeve, J., Box, J.E., 2005. Mapping daily snow/ice shortwave broadband albedo from Moderate Resolution Imaging Spectroradiometer (MODIS): the improved direct retrieval algorithm and validation with Greenland in situ measurement. J. Geophys. Res.-Atmos. 110, D10109.

Liang, S.L., Wang, K.C., Zhang, X.T., Wild, M., 2010. Review on estimation of land surface radiation and energy budgets from ground measurement, remote sensing and model simulations. IEEE J. Sel. Top. Appl. Earth Obs. Remote Sens. 3, 225–240.

Liang, S.L., Zhao, X., Liu, S., Yuan, W., Cheng, X., Xiao, Z., Zhang, X., Liu, Q., Cheng, J., Tang, H., Qu, Y., Bo, Y., Qu, Y., Ren, H., Yu, K., Townshend, J., 2013. A long-term Global land Surface Satellite (GLASS) data-set for environmental studies. Int. J. Digital Earth 6, 5–33.

Lyapustin, A., Wang, Y., Laszlo, I., Kahn, R., Korkin, S., Remer, L., Levy, R., Reid, J.S., 2011. Multiangle implementation of atmospheric correction (MAIAC): 2. Aerosol algorithm. J. Geophys. Res.-Atmos. 116, D03211.

Martonchik, J.V., Diner, D.J., Pinty, B., Verstraete, M.M., Myneni, R.B., Knyazikhin, Y., Gordon, H.R., 1998. Determination of land and ocean reflective, radiative, and biophysical properties using multiangle imaging. IEEE Trans. Geosci. Remote Sens. 36, 1266–1281.

Masek, J.G., Honzak, M., Goward, S.N., Liu, P., Pak, E., 2001. Landsat-7 ETM + as an observatory for land cover initial radiometric and geometric comparisons with Landsat-5 Thematic Mapper. Remote Sens. Environ. 78, 118–130.

Masek, J.G., Vermote, E.F., Saleous, N.E., Wolfe, R., Hall, F.G., Huemmrich, K.F., Gao, F., Kutler, J., Lim, T.K., 2006. A Landsat surface reflectance dataset for North America, 1990–2000. IEEE Geosci. Remote Sens. Lett. 3, 68–72.

Molling, C.C., Heidinger, A.K., Straka, W.C., Wu, X.Q., 2010. Calibrations for AVHRR channels 1 and 2: review and path towards consensus. Int. J. Remote Sens. 31, 6519–6540.

Muller, J.-P., Lopez, G., Watson, G., Shane, N., Kennedy, T., Yuen, P., Lewis, P., Fischer, J., Guanter, L., Domench, C., Preusker, R., North, P., Heckel, A., Danne, O., Kramer, U., Zuhlke, M., Brockmann, C., Pinnock, S., 2012. The ESA GlobAlbedo project for mapping the Earth's land surface albedo for 15 years from European sensors. In: IEEE Geoscience and Remote Sensing Symposium (IGARSS) 2012. IEEE, Munich, Germany.

O'Halloran, T.L., Law, B.E., Goulden, M.L., Wang, Z.S., Barr, J.G., Schaaf, C., Brown, M., Fuentes, J.D., Gockede, M., Black, A., Engel, V., 2012. Radiative forcing of natural forest disturbances. Glob. Chang. Biol. 18, 555–565.

Pinty, B., Roveda, F., Verstraete, M.M., Gobron, N., Govaerts, Y., Martonchik, J.V., Diner, D.J., Kahn, R.A., 2000. Surface albedo retrieval from Meteosat - 1. Theory. J. Geophys. Res.-Atmos. 105, 18099–18112.

Popp, C., Wang, P., Brunner, D., Stammes, P., Zhou, Y., Grzegorski, M., 2011. MERIS albedo climatology for FRESCO + O-2 A-band cloud retrieval. Atmos. Meas. Tech. 4, 463–483.

Qu, Y., Liu, Q., Liang, S., Wang, L., Liu, N., Liu, S., 2014. Direct-estimation algorithm for mapping daily land-surface broadband albedo from MODIS data. IEEE Trans. Geosci. Remote Sens. 52, 907–919.

Riihela, A., Manninen, T., Laine, V., Andersson, K., Kaspar, F., 2013. CLARA-SAL: a global 28 yr timeseries of Earth's black-sky surface albedo. Atmos. Chem. Phys. 13, 3743–3762.

Roman, M.O., Schaaf, C.B., Woodcock, C.E., Strahler, A.H., Yang, X.Y., Braswell, R.H., Curtis, P.S., Davis, K.J., Dragoni, D., Goulden, M.L., Gu, L.H., Hollinger, D.Y., Kolb, T.E., Meyers, T.P., Munger, J.W., Privette, J.L., Richardson, A.D., Wilson, T.B., Wofsy, S.C., 2009. The MODIS (collection V005) BRDF/albedo product: assessment of spatial representativeness over forested landscapes. Remote Sens. Environ. 113, 2476–2498.

Roman, M.O., Schaaf, C.B., Lewis, P., Gao, F., Anderson, G.P., Privette, J.L., Strahler, A.H., Woodcock, C.E., Barnsley, M., 2010. Assessing the coupling between surface albedo derived from MODIS and the fraction of diffuse skylight over spatially-characterized landscapes. Remote Sens. Environ. 114, 738–760.

Roman, M.O., Gatebe, C.K., Shuai, Y., Wang, Z., Gao, F., Masek, J.G., He, T., Liang, S., Schaaf, C.B., 2013. Use of in situ and airborne multiangle data to assess MODIS- and Landsat-based estimates of directional reflectance and albedo. IEEE Trans. Geosci. Remote Sens. 51, 1393–1404.

Schaaf, C.B., Gao, F., Strahler, A.H., Lucht, W., Li, X.W., Tsang, T., Strugnell, N.C., Zhang, X.Y., Jin, Y.F., Muller, J.P., Lewis, P., Barnsley, M., Hobson, P., Disney, M., Roberts, G., Dunderdale, M., Doll, C., d'Entremont, R.P., Hu, B.X., Liang, S.L., Privette, J.L., Roy, D., 2002. First operational BRDF, albedo nadir reflectance products from MODIS. Remote Sens. Environ. 83, 135–148.

Shuai, Y.M., Schaaf, C.B., Strahler, A.H., Liu, J.C., Jiao, Z.T., 2008. Quality assessment of BRDF/albedo retrievals in MODIS operational system. Geophys. Res. Lett. 35, L05407.

Shuai, Y.M., Masek, J.G., Gao, F., Schaaf, C.B., 2011. An algorithm for the retrieval of 30-m snow-free albedo from Landsat surface reflectance and MODIS BRDF. Remote Sens. Environ. 115, 2204–2216.

Shuai, Y.M., Masek, J.G., Gao, F., Schaaf, C.B., He, T., 2014. An approach for the long-term 30-m land surface snow-free albedo retrieval from historic Landsat surface reflectance and MODIS-based a priori anisotropy knowledge. Remote Sens. Environ.

152, 467–479.

Stroeve, J.C., Box, J.E., Haran, T., 2006. Evaluation of the MODIS (MOD10A1) daily snow albedo product over the Greenland ice sheet. Remote Sens. Environ. 105, 155–171.

Stroeve, J., Box, J.E., Wang, Z., Schaaf, C., Barrett, A., 2013. Re-evaluation of MODIS MCD43 Greenland albedo accuracy and trends. Remote Sens. Environ. 138, 199–214.

Tan, B., Woodcock, C.E., Hu, J., Zhang, P., Ozdogan, M., Huang, D., Yang, W., Knyazikhin, Y., Myneni, R.B., 2006. The impact of gridding artifacts on the local spatial properties of MODIS data: implications for validation, compositing, and band-to-band registration across resolutions. Remote Sens. Environ. 105, 98–114.

Thome, K., Markham, B., Barker, J., Slater, P., Biggar, S., 1997. Radiometric calibration of Landsat. Photogramm. Eng. Remote. Sens. 63, 853–858.

Tucker, C.J., Grant, D.M., Dykstra, J.D., 2004. NASA's global orthorectified landsat data set. Photogramm. Eng. Remote. Sens. 70, 313–322.

Vanderhoof, M., Williams, C.A., Shuai, Y., Jarvis, D., Kulakowski, D., Masek, J., 2014. Albedo-induced radiative forcing from mountain pine beetle outbreaks in forests, south-central Rocky Mountains: magnitude, persistence, and relation to outbreak severity. Biogeosciences 11, 563–575.

Vermote, E.F., Tanre, D., Deuze, J.L., Herman, M., Morcrette, J.J., 1997. Second simulation of the satellite signal in the solar Spectrum, 6S: an overview. IEEE Trans. Geosci. Remote Sens. 35, 675–686.

Vermote, E., Justice, C.O., Breon, F.M., 2009. Towards a generalized approach for correction of the BRDF effect in MODIS directional Reflectances. IEEE Trans. Geosci. Remote Sens. 47, 898–908.

Wang, Z., Schaaf, C.B., Chopping, M.J., Strahler, A.H., Wang, J., Roman, M.O., Rocha,

A.V., Woodcock, C.E., Shuai, Y., 2012. Evaluation of Moderate-resolution Imaging Spectroradiometer (MODIS) snow albedo product (MCD43A) over tundra. Remote Sens. Environ. 117, 264–280.

Wang, D., Liang, S.L., He, T., Yu, Y., 2013. Direct estimation of land surface albedo from VIIRS data: algorithm improvement and preliminary validation. J. Geophys. Res.-Atmos. 118, 12577–12586.

Wang, D., Liang, S.L., He, T., Yu, Y., Schaaf, C., Wang, Z., 2015. Estimating daily mean land surface albedo from MODIS data. J. Geophys. Res. Atmos. 120, 4825–4841.

Wang, Z., Erb, A., Schaaf, C., Sun, Q., Liu, Y., Yang, Y., Shuai, Y., Casey, K.A., Roman, M., 2016. Early spring post-fire snow albedo dynamics in high latitude boreal forests using Landsat-8 OLI data. Remote Sens. Environ. 185, 71–83.

Woodcock, C.E., Allen, R., Anderson, M., Belward, A., Bindschadler, R., Cohen, W., Gao, F., Goward, S.N., Helder, D., Helmer, E., Nemani, R., Oreopoulos, L., Schott, J., Thenkabail, P.S., Vermote, E.F., Vogelmann, J., Wulder, M.A., Wynne, R., Team, L.S., 2008. Free access to Landsat imagery. Science 320, 1011.

Yang, F.L., Mitchell, K., Hou, Y.T., Dai, Y.J., Zeng, X.B., Wang, Z., Liang, X.Z., 2008. Dependence of land surface albedo on solar zenith angle: observations and model parameterization. J. Appl. Meteorol. Climatol. 47, 2963–2982.

Zhou, Y.Y., Weng, Q.H., Gurney, K.R., Shuai, Y.M., Hu, X.F., 2012. Estimation of the relationship between remotely sensed anthropogenic heat discharge and building energy use. ISPRS J. Photogramm. Remote Sens. 67, 65–72.

Zhou, Y., Wang, D.D., Liang, S.L., Yu, Y.Y., He, T., 2016. Assessment of the Suomi NPP VIIRS land surface albedo data using station measurements and high-resolution albedo maps. Remote Sens. 8, 137.